# CHAPTER 4

# 4. RESULTS AND DISCUSSION

## 4.1 Synthesis and Catalytic Activity of Cu-Cr-O-$TiO_2$ Composites on Thermal Decomposition of Ammonium Per-chlorate:

This section discusses and presents the results of the characterization of Cu-Cr-O.n$TiO_2$ composite oxides using varying concentrations of $TiO_2$ with the Cu-Cr-O. Their effects on the thermal decomposition rate of ammonium perchlorate are also discussed.

In the present work simultaneous effects of copper chromites and $TiO_2$ catalysts on the thermal decomposition of AP have been investigated. Several methods such as co-precipitation, solid state synthesis, the ceramic method, the solution combustion method, the hydrothermal method and sol–gel methods have previously been reported for the preparation of the catalysts. Due to better control of homogeneity and the ease of the procedure, the sol–gel method was used in this work [Yan *et al.* 2009]. Thus, after the successful preparation of different concentrations of $TiO_2$-doped copper chromite compositions, i.e. Cu–Cr–O.n$TiO_2$ (n = 0.5, 0.7 and 0.9), calcined at two different temperatures, 300 and 1050°C, the catalyst was introduced into AP to enhance its burn rate. The results of various investigations conducted for this purpose are discussed in the following section.

### 4.1.1 Thermo-gravimetric Analysis:

Figure.4.1 shows the TGA curve of catalyst precursor (Cu-Cr-O-citric acid). The curve consists of three regions of weight loss within the temperature range of 30 -1000°C. The first region (30-180°C) shows the weight loss of 6.6% due to removal of surface moisture. Second region (180-580°C) shows the major weight loss of 54.2% and is attributed to the removal of volatile organics.

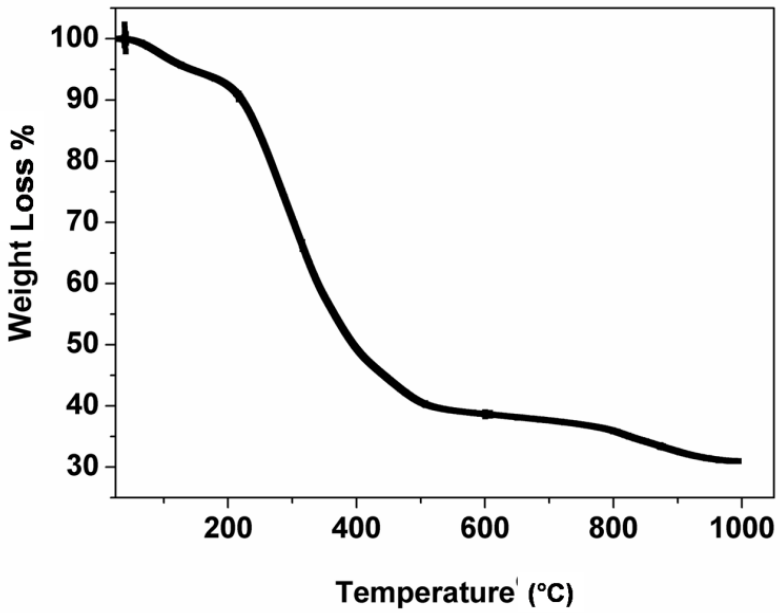


Fig.4.1: TGA Curve of Catalyst Precursor (Cu-Cr-O-citric acid).

The curve consists of three regions of weight loss within the temperature range of 30 -1000 °C. Partial decomposition of nitrate bonds and formation of intermediate complexes of copper, chromium, titanium oxide and nitrates is accounting the weight loss of 7% in the third segment (580-980°C). Beyond the temperature 980°C, the curve looks almost parallel to temperature axis which shows no noticeable weight loss occurs.

### 4.1.2 X-Ray Diffraction Analysis:

Figure.4.2 shows the typical XRD patterns of the (a) Cu-Cr-O.0.5$TiO_2$, (b) Cu-Cr-O.0.7$TiO_2$ and (c) Cu-Cr-O.0.9$TiO_2$ catalysts calcined at 300°C for 3 h. XRD patterns show the diffraction peaks appearing only due to $TiO_2$ (JCPDS file No. 46-1238).

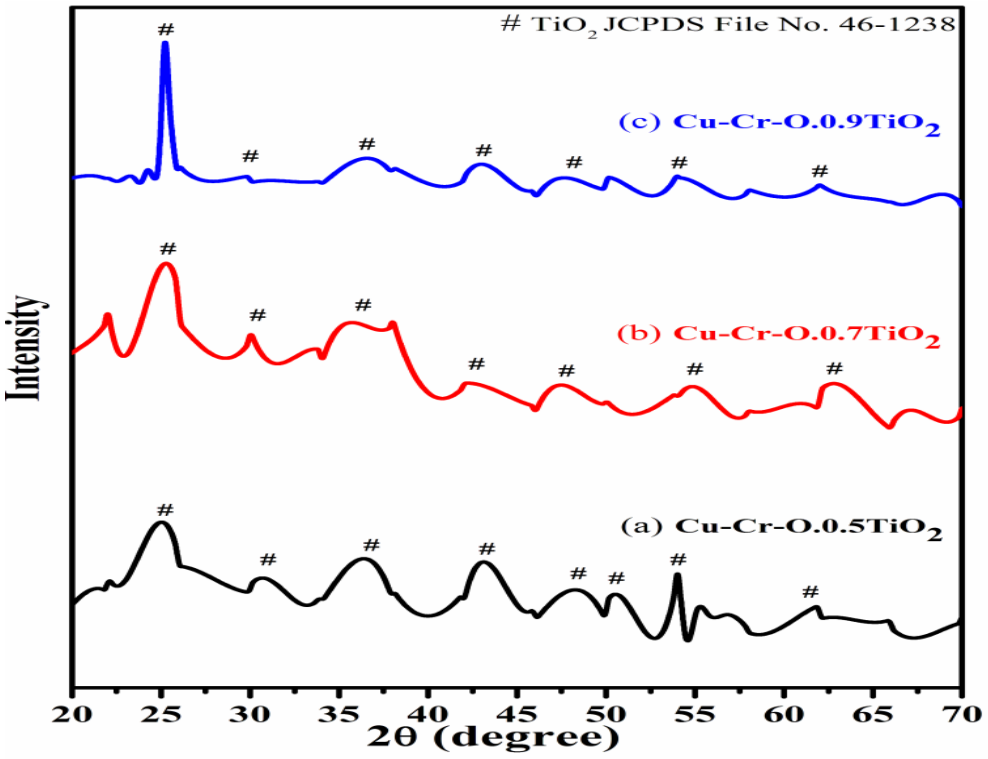


Fig. 4.2: XRD Patterns of (a) Cu-Cr-O.0.5$TiO_2$, (b) Cu-Cr-O.0.7$TiO_2$ and (c) Cu-Cr-O.0.9$TiO_2$ Catalysts Calcined at 300°C

This may happen due to the crystallization of $TiO_2$ in the mixed state at around 300°C and rest of the compounds such as $CuCr_2O_4$, $Cu_2Cr_2O_4$, $Cu_2O$ are not found to be crystallized at this temperature hence show the absence of diffraction peaks. As the calcination temperature is increased up to 1050 °C, the transformation of the composite materials ($CuCr_2O_4$, $Cu_2Cr_2O_4$, $Cu_2O$) from amorphous to crystalline phase takes place due to well known crystallization temperature of Cu-Cr-O at 700 °C. Figures 4.3 (a-c) show XRD profiles of the various compositions of oxides calcined at 1050 °C for 3 h.

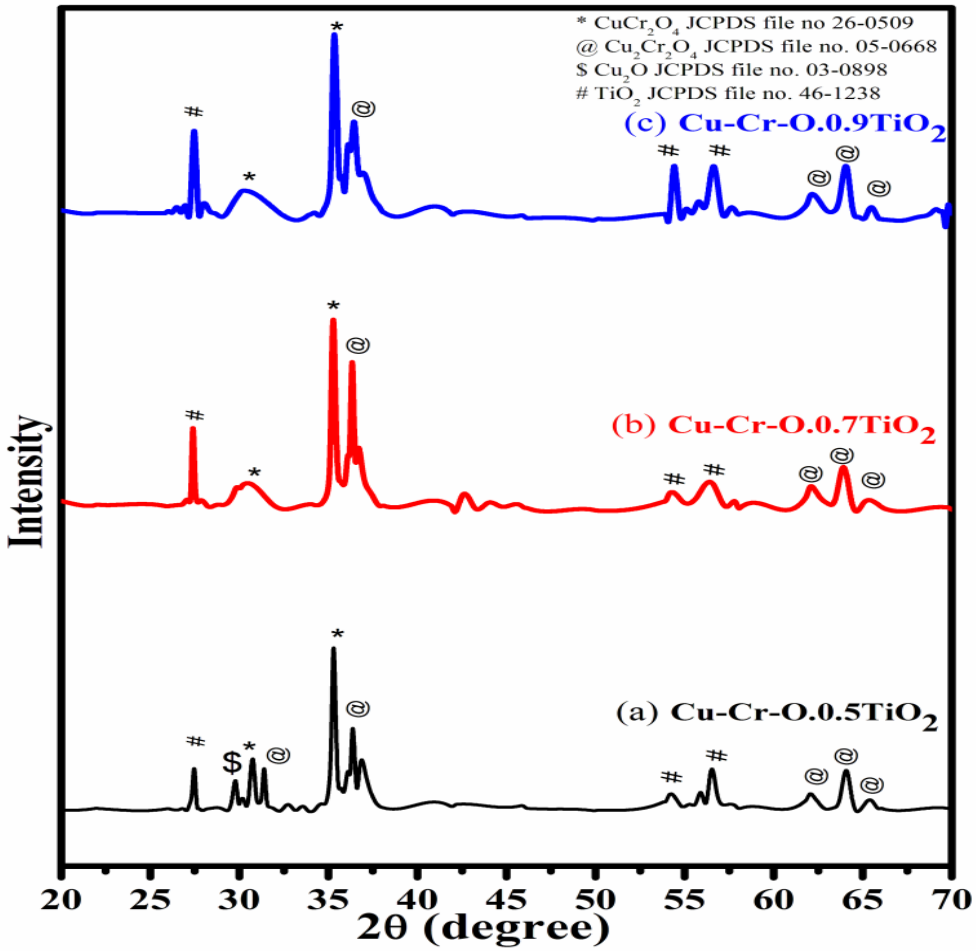


Fig. 4.3: XRD Patterns of (a) Cu-Cr-O.0.5$TiO_2$, (b) Cu-Cr-O.0.7$TiO_2$ and (c) Cu-Cr-O.0.9$TiO_2$ Catalysts Calcined at 1050°C

The diffraction patterns showed the peaks due to $CuCr_2O_4$, $Cu_2Cr_2O_4$ and $Cu_2O$ along with $TiO_2$. The prominent diffraction peaks of $CuCr_2O_4$ (JCPDS file no 26-0509) appeared at the diffraction angle (2θ) of 30.76° and 35.31°. The diffraction peaks of $Cu_2Cr_2O_4$ are appeared at the diffraction angle of 31.4°, 36.38°, 62.06°, 64.08° and 65.40° (JCPDS file no. 05-0668). Whereas, the presence of $Cu_2O$ is noticed due to its characteristic peak at 29.78° (JCPDS file no. 03-0898). Only three diffraction peaks at 27.48°, 54.24° and 56.54°of $TiO_2$ are observed for the compositions calcined at 1050°C.

### 4.1.4 Fourier Transforms Infrared Spectroscopic Analysis:

Figures 4.4 (a-c) show the typical FT-IR spectra of Cu-Cr-O.0.5$TiO_2$, Cu-Cr-O.0.7$TiO_2$ and Cu-Cr-O.0.9$TiO_2$ calcined at 300 °C n for 3 h. Figures 4.5 (a-c) show the FT-IR spectra of these mixed oxides at 1050 °C for the same duration. The respective spectra of mixed compositions calcined at 300 °C (Fig. 4.4) are quite different from the spectra of the samples calcined at 1050 °C (Fig. 4.5). It is interesting to note that most of the absorption bands (8 out of 10) have disappeared dramatically at higher temperature. Such dramatic vanishing of absorption bands occurred due to the effect of calcination temperature on the phase composition of these mixed oxides. The crystallization temperature Cu-Cr-O is 700°C, below which the oxides are in amorphous state showing similar IR pattern for 300°C. No spectroscopic changes are observed due to varying the concentration of $TiO_2$ on calcinations either at 300°C or at 1050°C. One of the strong peaks observed at wavenumber 1628 $cm^{-1}$ is due the $\nu_2$ bending mode of H–O–H in $H_2O$ [Mishra *et al.* 2012 ; 2016]. The position of this band may vary by ±10 $cm^{-1}$ depending on the host molecule to which $H_2O$ is attached. The absorption band appearing at 1414 $cm^{-1}$ may be attributed to the symmetric vibration of surface hydroxyl group. A medium shoulder appearing at 1282 $cm^{-1}$ was attributed to the coupled bending and stretching vibrations of $COO^-$ of citric acid. Notably, this band has appeared in IR patterns of the samples calcined at 300°C not in the samples calcined at 1050 °C. The dramatic disappearance of this band in the samples fired at higher temperature was due to the reason that citric acid has its melting point at 310°C which is just above the 300 °C. That is why the citric acid is not destroyed at 300°C, However, at 1050 °C citric acid is destroyed completely resulting in the absence of the associated bands or any trace at this temperature. The peaks at 1058 $cm^{-1}$ can be attributed to C-H bending vibration of citric acid. However, a strong absorption band appearing at 1555 $cm^{-1}$ is assigned to C-C or C-O

stretching. These bands also appear at lower temperatures below crystallization Cu-Cr-O but not in the IR of the samples calcined at 1050 °C due to destruction of citric acid at higher temperature. The absorption bands at 721, 793 and 890 $cm^{-1}$ may be attributed to the different vibrational modes of $TiO_2$. $TiO_2$ exhibits strong absorption in the range 600-890 $cm^{-1}$ when treated with some additive metal ions.

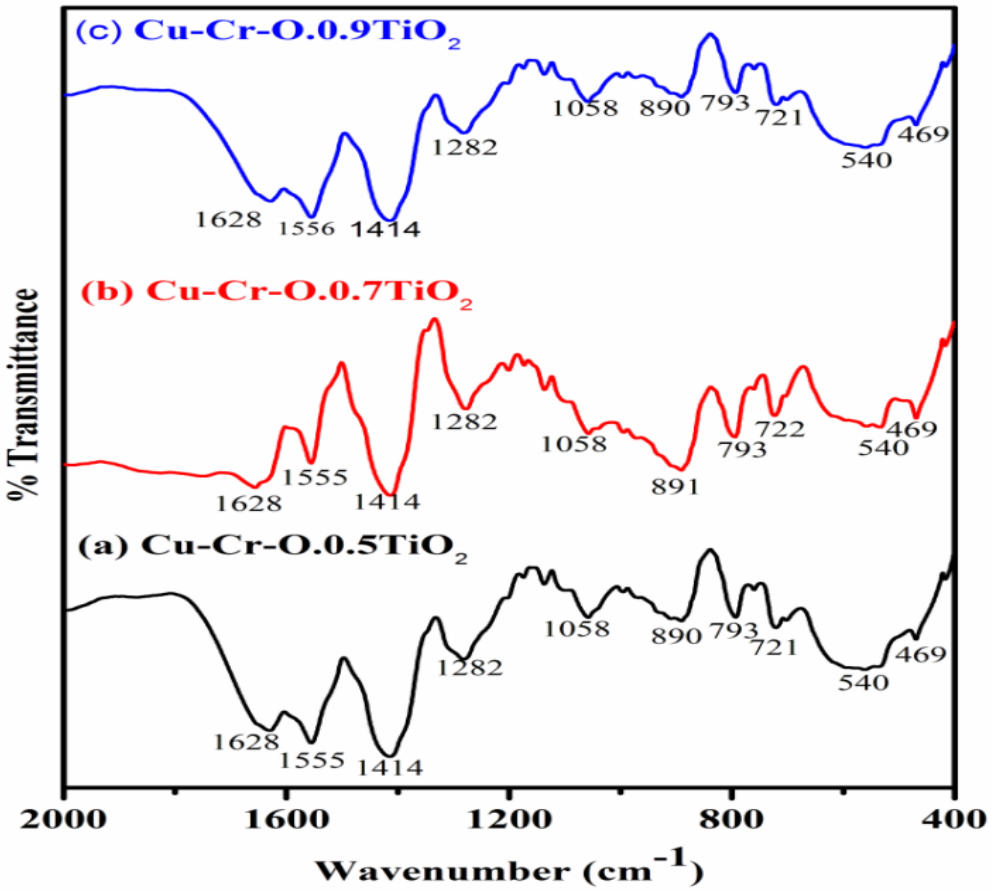


Fig. 4.4: FT- IR spectrum of Synthesized Catalysts Calcined 300°C

The broad band centered at 540 $cm^{-1}$ in IR spectra is attributed to the characteristic vibrational band (asymmetric) of Cu-O in CuO. This band also contains the contribution due to stretching bands of Cu-O-Cr. These spectra show a strong shoulder at 469 $cm^{-1}$ assigned to Ti-O asymmetric stretching vibrations. The amorphous and crystalline nature of the formed

compounds are confirmed from the FT-IR spectrum shown in Fig. 4.4(a-c) and Fig. 4.5(a-c) which are in line with the XRD results.

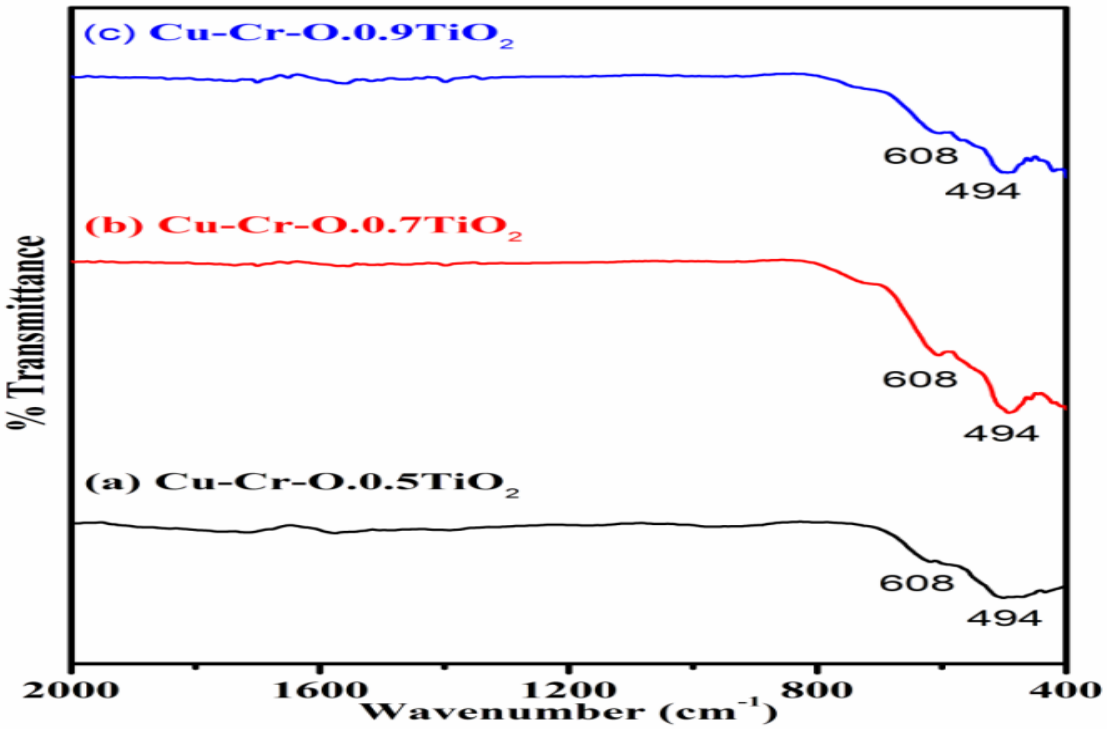


Fig. 4.5: FT- IR Spectrum of Synthesized Catalysts Calcined 1050°C

IR spectroscopy confirms the formation of intermediate complex compounds in the amorphous phase as explained by the XRD results.

### 4.1.5 Scanning Electron Microscopic Analysis:

Figure.4.6 shows the typical SEM images of the catalyst samples (a) Cu-Cr-O.0.5$TiO_2$, (b) Cu-Cr-O.0.7$TiO_2$ and (c) Cu-Cr-O.0.9$TiO_2$ calcined at 300°C for 3 h. As shown in the micrographs, the particles have grown in spherical and needle like structures with diameter up to 180 nm and 50 nm, respectively. However, Fig. 4.7(a-c) exhibit the respective microstructures of the same catalyst samples calcined at 1050°C. Whilst the images shown in Fig.4.6, exhibit the formation of nanoparticles of the size 20-100 nm, the images in Fig.4.7 (a-c) show that cuboids-

like particles of size below 1 μm developed under heat treatment. The shape of the synthesized catalysts particles is more regular and bigger in size as compared with the samples calcined at 300°C. This transformation of surface morphology with the increase in temperature (from 300 to 1050°C) is very interesting. The particle size of the same sample has changed from nano to micro order due to the fusion of the particles to each other at the higher temperature (1050°C) minimizing the surface energy minimum. Moreover, the formation of some new phases occurred at 1050°C. The bigger size of the particles leads to the reduction in specific surface area.

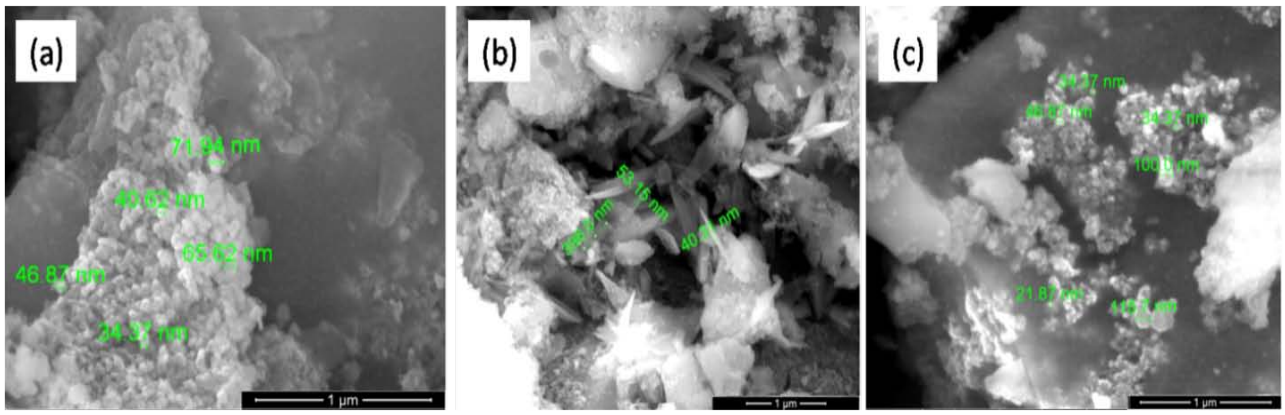


Fig. 4.6: SEM Images of Synthesized Catalysts Calcined at 300°C

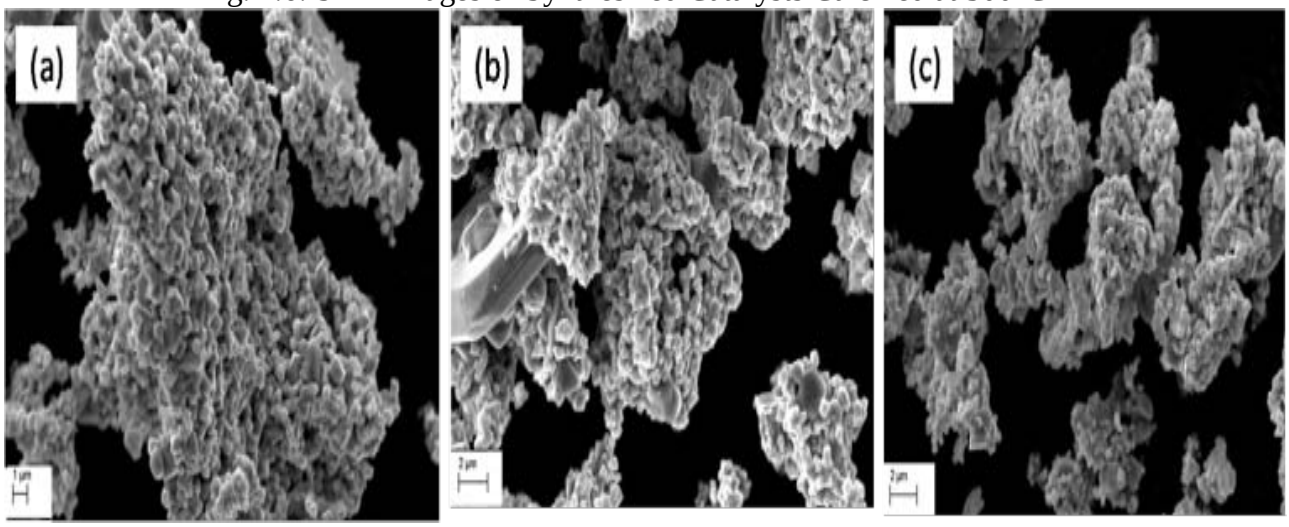


Fig. 4.7: SEM Images of Synthesized Catalysts Calcined at 1050°C

### 4.1.6 Transmission Electron Microscopic (TEM) Analysis:

Figure 4.8 shows the TEM image of Cu–Cr–O.0.7$TiO_2$ calcined at 300°C. The TEM results are consistent with the previously observed crystallographic, spectroscopic and microstructural characterization results of all the compositions calcined individually at 300°C and 1050°C.

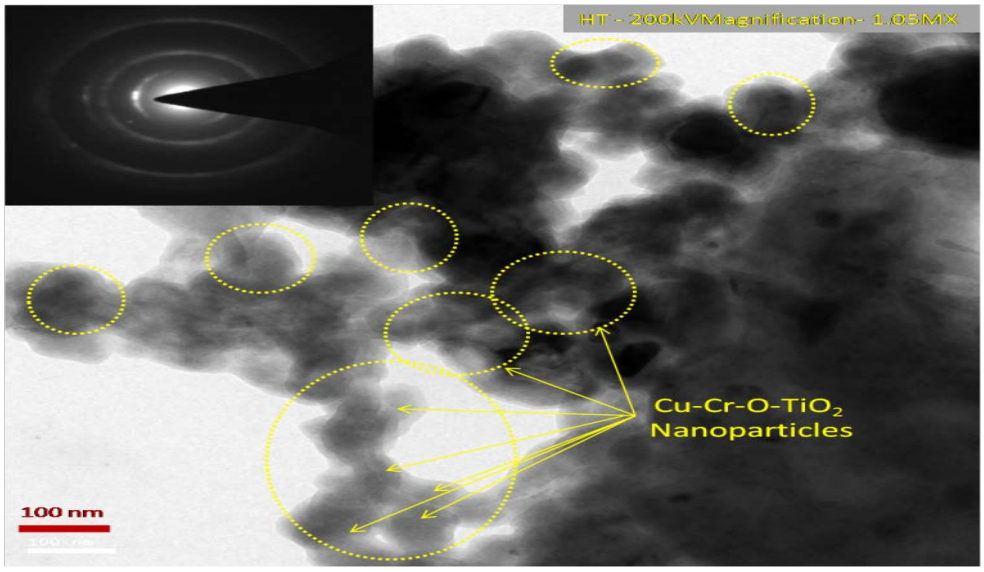


Fig. 4.8: TEM Image of Cu-Cr-O.0.7$TiO_2$ Calcined at 300 °C with SAED Pattern

The catalyst sample Cu–Cr–O–$TiO_2$ calcined at 300°C is structurally residue citrate superb for further application in the desired experiment. The Cu–Cr–O–$TiO_2$ particles sized around 100 nm can be seen easily in the yellow dotted rings as shown by yellow arrows. The TEM image confirms that the diffusion of particles does not occur at 300°C, however it happens at the higher temperature of 1050°C as shown in Fig. 4.7.

### 4.1.7 Energy Dispersive X-ray (EDX) Analysis:

Figures 4.9 & 4.10 show the EDAX spectra of synthesized catalysts calcined at different temperature 300 and 1050 °C for 3h and the elemental compositions of the catalysts are shown in Table 4.1

**Table 4.1:** Elemental Composition (Weight %) of Different Cu-Cr-O-$TiO_2$ Composites Calcined at 300 and 1050°C

| **300 °C** | | | | **1050 °C** | | |
|---|---|---|---|---|---|---|
| **Elements** | **Cu-Cr-O.0.5$TiO_2$** | **Cu-Cr-O.0.5$TiO_2$** | **Cu-Cr-O.0.5$TiO_2$** | **Cu-Cr-O.0.5$TiO_2$** | **Cu-Cr-O.0.5$TiO_2$** | **Cu-Cr-O.0.5$TiO_2$** |
| O | 15.02 | 39.72 | 14.93 | 34.39 | 41.81 | 33.2 |
| Ti | 8.09 | 13.28 | 19.37 | 8.51 | 14.03 | 15.28 |
| Cr | 17.49 | 30.67 | 44.91 | 34.25 | 27.37 | 30.64 |
| Cu | 59.40 | 16.33 | 20.79 | 22.85 | 16.08 | 20.88 |

This analysis confirmed the presence of copper, chromium, titanium and oxygen. The increasing weight % of oxygen with increase in the temperature may occur due to the transformation of intermediate compounds of Cu-Cr-O-Citric acid into metal oxides. Interestingly, CuO has already shown its presence in XRD patterns of the samples calcined at 1050 °C not in the samples calcined at 300 °C.

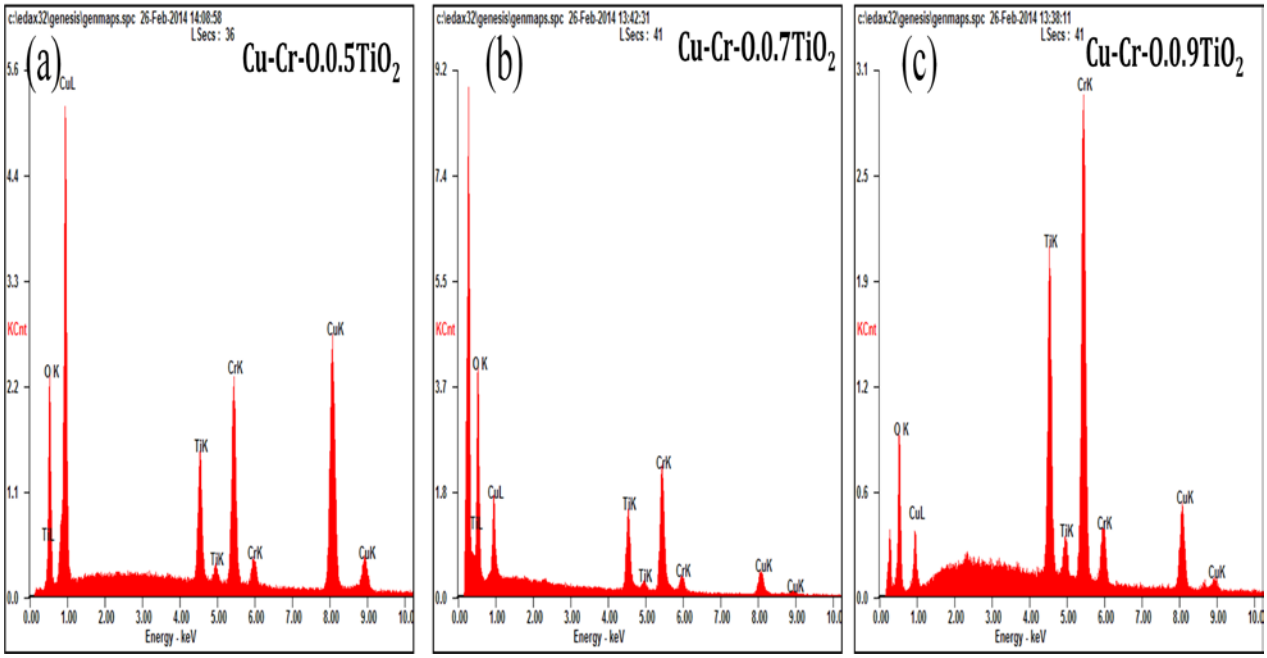


Fig. 4.9: EDAX Spectrum of (a) Cu-Cr-O.0.5$TiO_2$, (b) Cu-Cr-O.0.7$TiO_2$ and (c) Cu-Cr-O.0.9$TiO_2$ Calcined at 300 °C

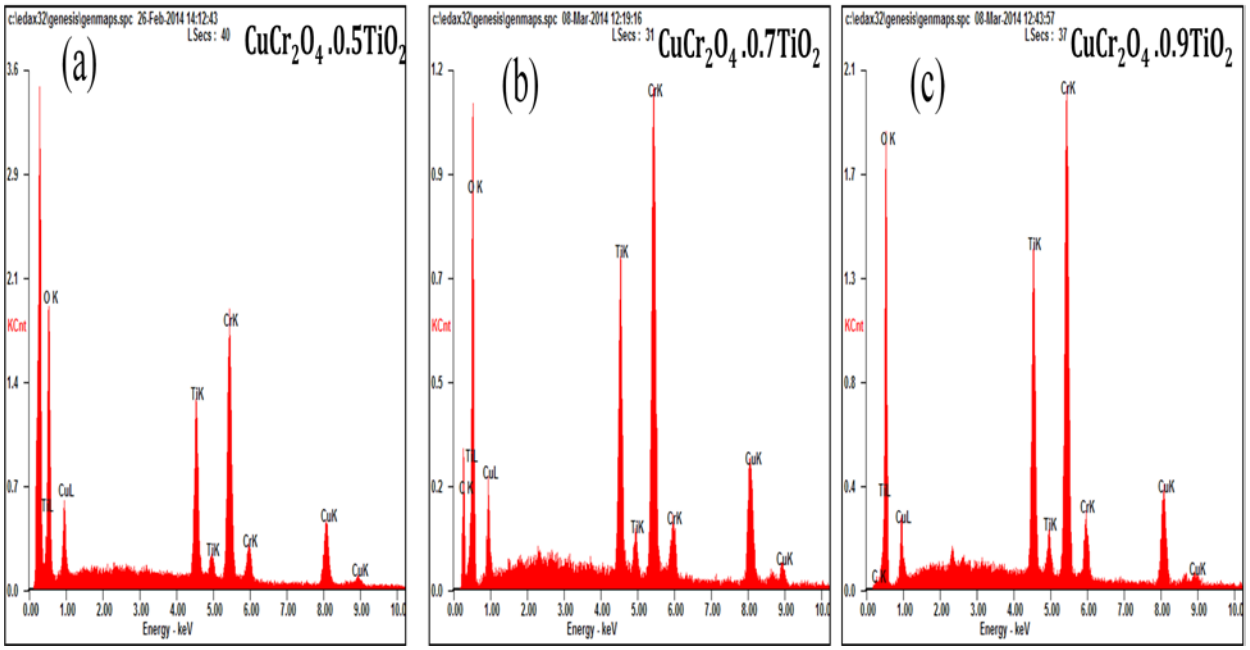


Fig. 4.10: EDAX spectrum of (a) Cu-Cr-O.0.5$TiO_2$, (b) Cu-Cr-O.0.7$TiO_2$ and (c) Cu-Cr-O.0.9$TiO_2$ calcined at 1050°C

### 4.1.8 Catalytic Activity of Catalyst on Thermal Decomposition of AP:

The synthesized nano-composites of Cu-Cr-O.n$TiO_2$ with varying molar ratios of $TiO_2$ are explored as additives to know their influence on the thermal decomposition of AP. Figure. 4.11 shows the DTA curves of (a) $AP_{300\mu}$ and (b) $AP_{45\mu}$ of two different particle sizes 300 and 45 µm respectively. Examination of curves clearly shows that the decomposition pattern of AP strongly depends on particle size, resulting in step-wise energy release. Figure 4.12 exhibits the corresponding % weight loss of the same samples. In Fig.4.11, the endothermic peak for both the samples appeared at 250°C which may be due to the crystallographic transformation of AP from orthorhombic to cubic.

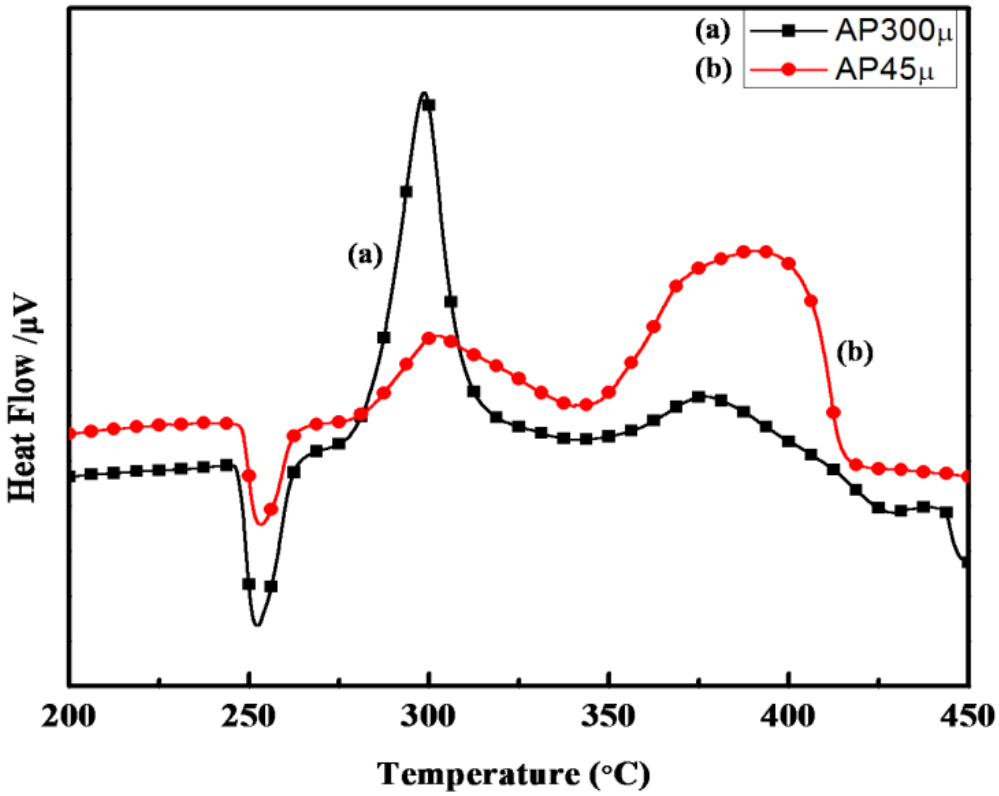


Fig.4.11: DTA Curves of (a) $AP3_{00\mu}$ & (b) $AP_{45\mu}$

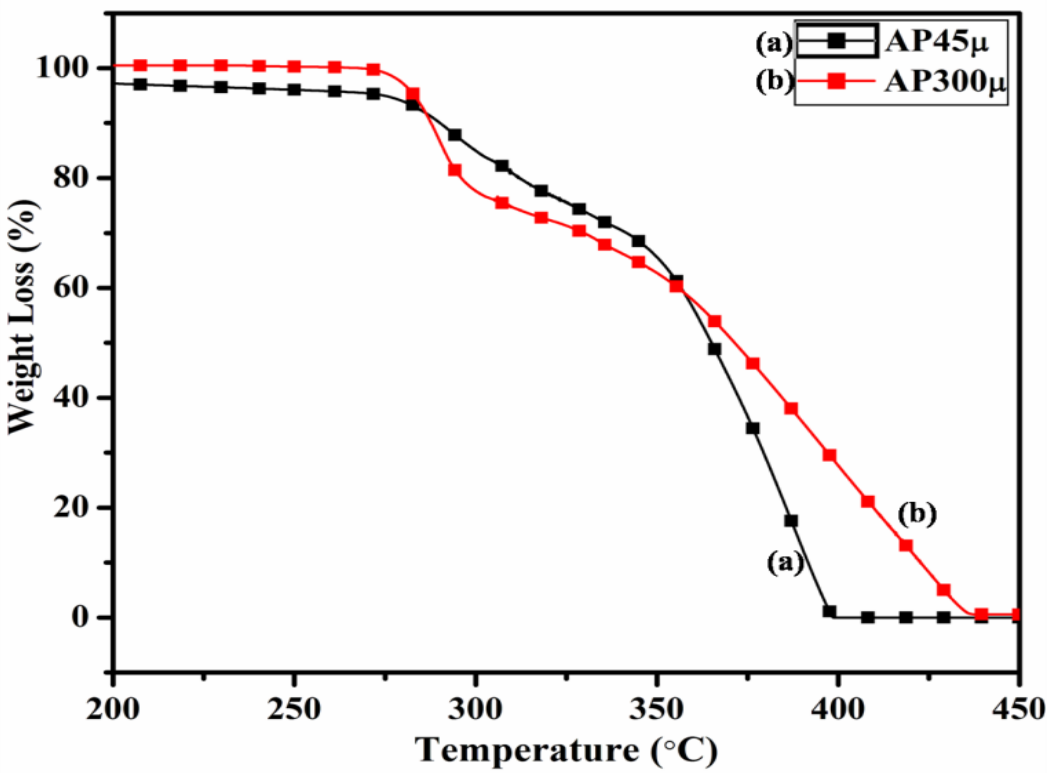


Fig.4.12: TGA curves of (a) $AP_{45\mu}$ & (b) $AP_{300\mu}$

The decomposition peak at 302°C is attributed to the formation of intermediates such as $NH_4^+$ and $HClO_4^-$ which is reported as LTD [Davenas, 1992]. The peak at 385 °C signifies the complete decomposition of volatile product into $H_2O$, HCl, $N_2$, $H_2$ and $O_2$ and it is termed as HTD. Figure 4.13 and Figure 4.14 show the decomposition (DTA) and % weight loss (TGA) patterns of $AP_{45\mu}$ modified with industrial ACR (Cu-Cr-O), respectively. A significant change can be observed in thermo-gram as shown in Fig. 4.11. An endothermic peak appearing at 250 °C in pure AP has shifted towards lower temperature and appeared at 245 °C which is well known crystallographic change temperature for AP. The exothermic peak appearing at 302 °C has shifted to 310 °C with a new proximal peak at 330°C probably due to decomposition of additives signifying the increase in decomposition energy.

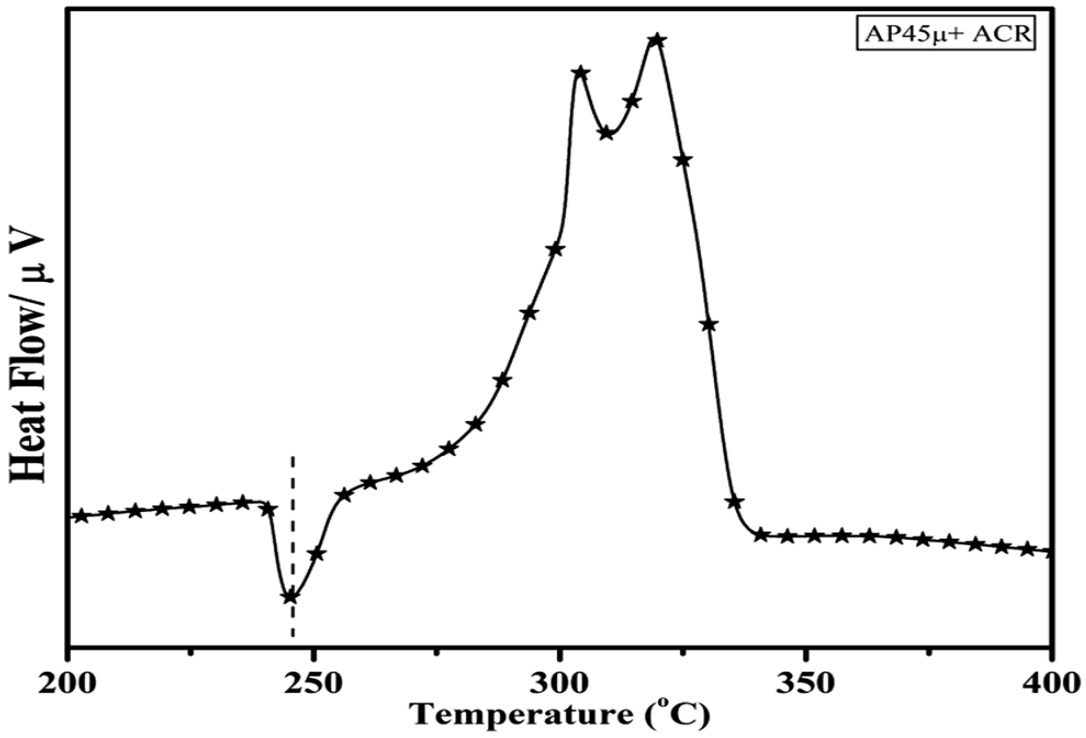


Fig.4.13: DTA Curve of $AP_{45\mu}$ Modified with Industrial ACR (Cu–Cr–O)

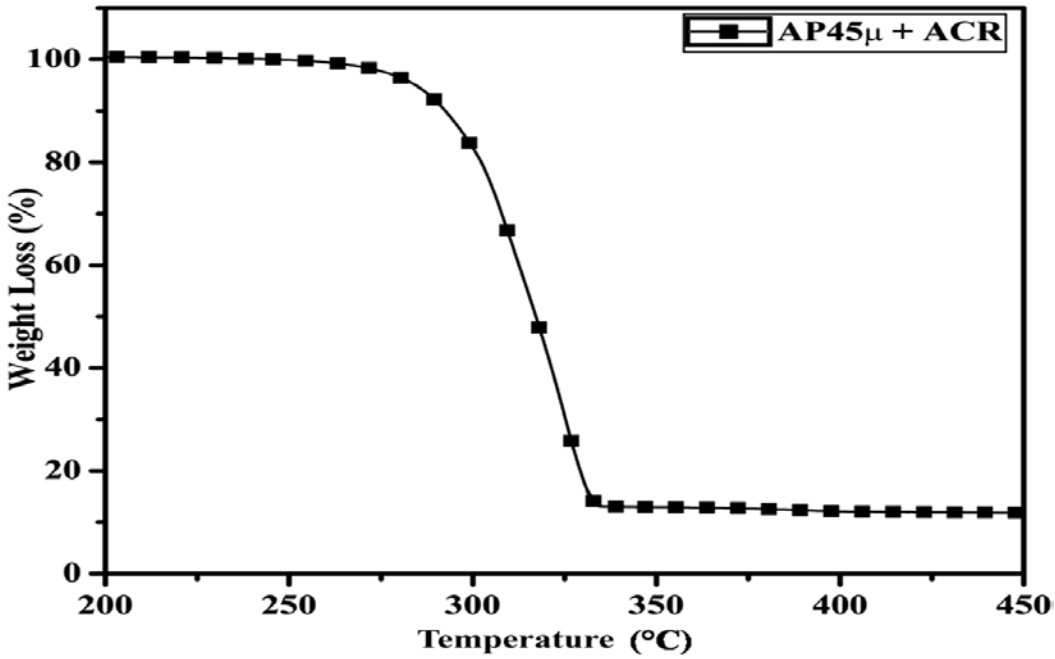


Fig. 4.14: TGA Curve of $AP_{45\mu}$ Modified with Industrial ACR (Cu–Cr–O)

The TGA thermogram shows three clear-cut stages of weight loss in which major weight loss has occurred in the second stage covering the range 285-335 °C. Thermograms shown in Fig. 4.15 (a and b) and Fig.4.16 (a and b) represent the DTA (decomposition characteristic) and TGA (% weight loss) of AP modified with prepared catalysts of Cu-Cr-O.0.n$TiO_2$ (n= (a) 0.5 and (b) 0.7) calcined at 300°C, respectively. The endothermic peak due to crystallographic change appears again at 245°C. A considerable improvement in decomposition characteristic is observed with the introduction of $TiO_2$ into the Cu-Cr-O with calcination at 300°C. The 0.7 mol % addition of $TiO_2$ into the Cu-Cr-O calcined at 300°C results in a single step sharp decomposition of AP at 306°C. The sharp and high intensity decomposition peak clearly depicts the significant improvement in decomposition energy as well as decomposition (burn) rate of the modified AP.

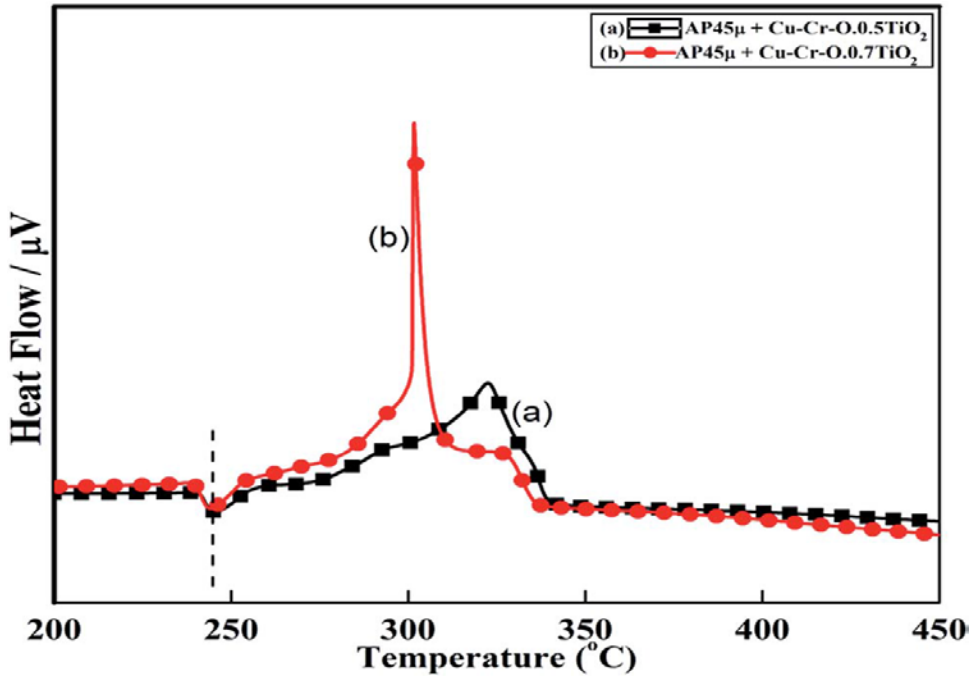


Fig. 4.15: DTA Curves of $AP_{45\mu}$ Modified with (a) Cu–Cr–O–0.5$TiO_2$ and (b) Cu–Cr–O–0.7$TiO_2$ Calcined at 300°C

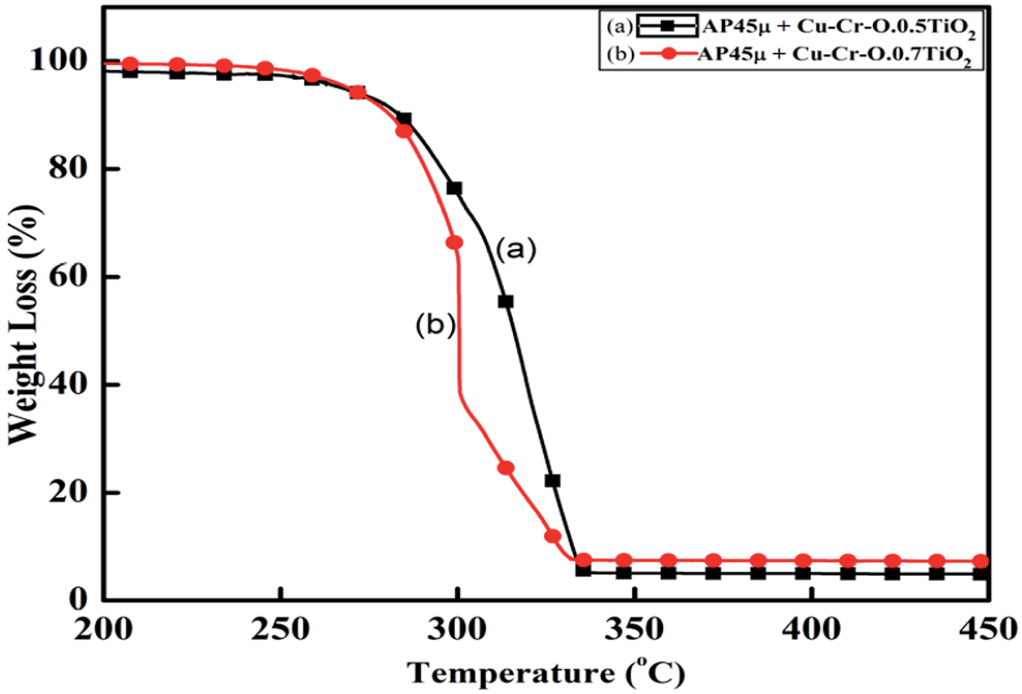


Fig. 4.16: TGA Curves of $AP_{45\mu}$ Modified with (a) Cu–Cr–O.0.5$TiO_2$ and (b) Cu–Cr–O.0.7$TiO_2$ Calcined at 300°C.

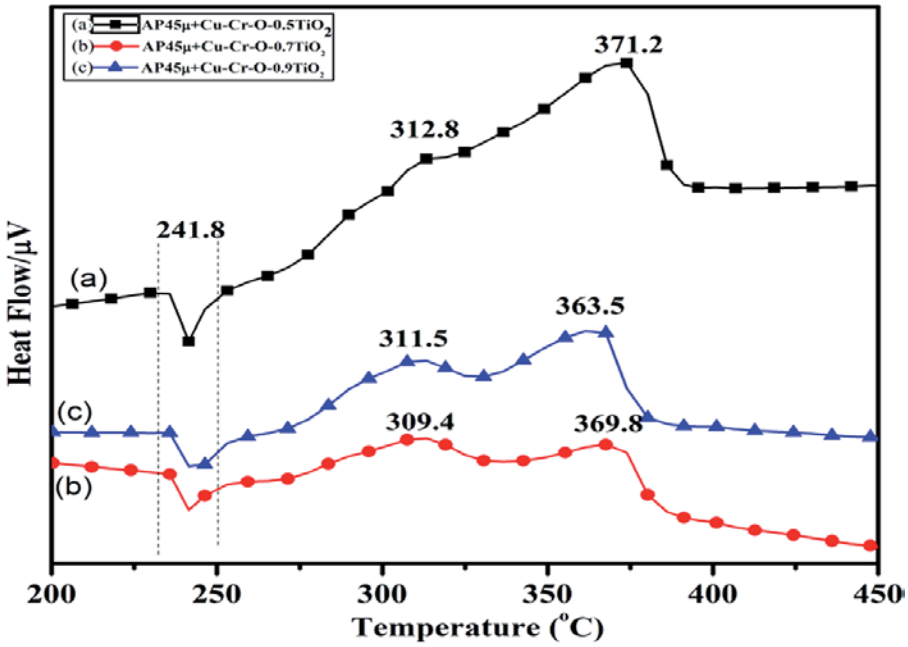


Fig. 4.17: DTA Curves of $AP_{45\mu}$ Modified with (a) Cu–Cr–O.0.5$TiO_2$, (b) Cu–Cr–O.0.7$TiO_2$ and (c) Cu–Cr–O.0.9$TiO_2$ Calcined at 1050°C

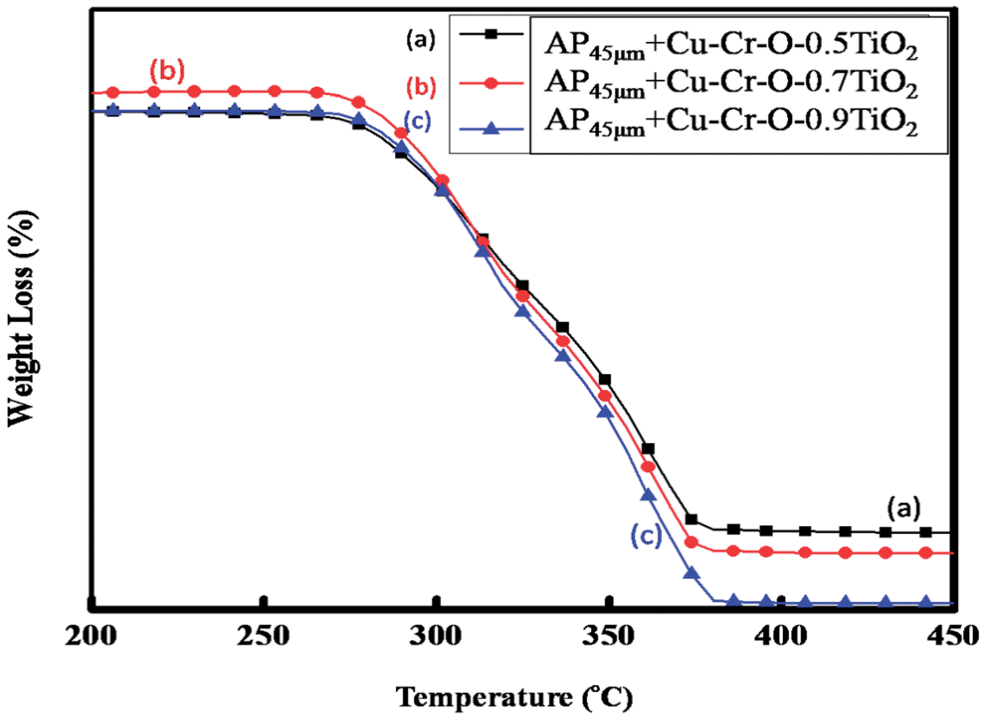


Fig. 4.18: TGA Curves of $AP_{45\mu}$ Modified with (a) Cu–Cr–O.0.5$TiO_2$, (b) Cu–Cr–O.0.7$TiO_2$ and (c) Cu–Cr–O.0.9$TiO_2$ Calcined at 1050°C

However, the introduction of 0.5 mol % $TiO_2$ into the Cu-Cr-O calcined at 300 °C gives a wide decomposition peak centered on 320 - 322 °C. It is important to note that catalysts are calcined at 300$^o$C before use as modifier in AP. Next, $TiO_2$ added catalyst samples are calcined at 1050$^o$C before use them as modifiers in AP.

Figures 4.17 (a-c) and 4.18 (a-c) exhibit the DTA and TGA patterns, respectively of $AP_{45\mu}$ modified with (a) Cu-Cr-O.0.5$TiO_2$, (b) Cu-Cr-O.0.7$TiO_2$ and (c) Cu-Cr-O.0.9$TiO_2$ calcined at 1050 °C. In these samples endothermic peak has appeared at 241°C rather than 245°C. The crystallographic change with temperature for any allotropic/polymorphic material is constant. However, it may be recorded at an increased temperature (2-5°C) in some certain circumstances like change in pressure or impurity, a measurement error and calibration fault. The

shift of 3 °C towards the lower side in crystallographic change temperature of pure AP may be due to one of these reasons. This endothermic peak attracts comparatively less interest than exothermic peaks in the present study. The onset of thermal decomposition of all these samples has been found within the temperature range of 300 °C to 313 °C. A brief summary of the decomposition temperature is shown in Table 4.1.2. The differential thermographs shown in Fig. 4.17 clearly depict the least effect of catalysts on thermal decomposition of ammonium per-chlorate.

**Table 4.2:** Decomposition Temperature of Pure AP, AP Modified with ACR and AP Modified with Different Compositions of Cu-Cr-O-$TiO_2$ Calcined at 300 and 1050°C

| Calcination Temp. of Cu-Cr-O-$TiO_2$ | Composition | Endothermic Peak Position (Single Peak) | Exothermic Peak Positions LTD (°C) | HTD (°C) |
|---|---|---|---|---|
| As synthesized<br><br>300 °C | $AP_{45\mu}/Ap_{300\mu}$ | 250 | 302 | 385 |
| | $AP_{45\mu}$ + ACR (Cu-Cr-O) | 245 | 310 & 330 | ---- |
| | $AP_{45\mu}$+ Cu-Cr-O-$0.5TiO_2$ | 245 | 320 & 322 | ---- |
| | $AP_{45\mu}$+ Cu-Cr-O-$0.7TiO_2$ | 245 | 306 | ---- |
| | | | | |
| 1050 °C | $AP_{45\mu}$+ Cu-Cr-O-$0.5TiO_2$ | 241.8 | 309.4 | 369.8 |
| | $AP_{45\mu}$+ Cu-Cr-O-$0.7TiO_2$ | 241.8 | 311.5 | 363.5 |
| | $AP_{45\mu}$+ Cu-Cr-O-$0.9TiO_2$ | 241.8 | 312.8 | 371.2 |

**Table 4.3:** Calibrated ΔH values for all the endothermic and exothermic peaks appeared in DTA of pure AP, AP modified with ACR and AP modified with different compositions of Cu-Cr-O-$TiO_2$ calcined at 300 and 1050°C

| **Calcination Temperature** | **Sample composition** | **Amount of sample ΔH (J/g)** | | | | |
|---|---|---|---|---|---|---|
| | | **Wt.(mg)** | **Endoth. Peak** | **Exhoth. Peak-1 LTD** | **Exhoth. Peak-2 HTD** | **Exhoth. Peak-3 HTD (II)** |
| **As Synthesized** | (a) $AP_{300\mu}$ | 12.457 | 87.2360 | -302.6432 | -173.6290 | -19.5203 |
| | (b) $AP_{45\mu}$ | 7.428 | 87.5459 | -211.8264 | -787.7451 | N/A |
| | $AP_{45\mu}$ + ACR (Cu-Cr-O) | 10.373 | 80.4025 | -27.3855 | -112.2612 | N/A |
| **300 °C** | (a) $AP_{45\mu}$ + Cu-Cr-O-0.5 $TiO_2$ | 16.000 | 83.2412 | -461.8651 | - 63.9416 | N/A |
| | (b) $AP_{45\mu}$ + Cu-Cr-O-0.7 $TiO_2$ | 11.107 | 82.8426 | -1411.2097 | N/A | N/A |
| **1050 °C** | (a) $AP_{45\mu}$ + Cu-Cr-O-0.5 $TiO_2$ | 8.115 | 56.1904 | -128.372 | - 452.176 | N/A |
| | (b) $AP_{45\mu}$ + Cu-Cr-O-0.7 $TiO_2$ | 5.032 | 58.4718 | -314.905 | -180.880 | N/A |
| | (c) $AP_{45\mu}$ + Cu-Cr-O-0.9 $TiO_2$ | 6.277 | 59.3275 | -123.219 | -186.66 | N/A |

However, results obtained in Fig. 4.15 show the maximum effect of catalyst (Cu-Cr-O.0.7$TiO_2$ calcined at 300°C) on the thermal decomposition of AP when compared with the results obtained in Fig. 4.13 and Fig. 4.17. The heat of reaction (i.e. calibrated delta (H) values are also estimated and given in Table 4.3. A careful examination of the table shows the highest value (-1411.2097) for the AP modified with Cu-Cr-O.0.7$TiO_2$ calcined at 300°C. Table 4.3 also shows the amount of the sample used in the characterization of thermal decomposition behavior. Thus

the sample Cu-Cr-O.0.7$TiO_2$ calcined at 300°C is very much efficient (best) catalyst compared with other laboratory prepared samples calcined at 1050°C as well as industrial ACR (Cu-Cr-O).

The decomposition behavior with and without the presence of the synthesized catalyst materials obtained from the DTA technique and are shown in the Fig. 4.11, Fig.4.13, Fig.4.15 and Fig.4.17. The first peak in each the figure is observed in the temperature range of 230 °C to 240 °C, which is endothermic in nature. This phenomenon can be attributed to the crystallographic change of AP from orthorhombic to cubic. The second decomposition is observed at the temperature of 310°C and is assigned as low the temperature decomposition (LTD) accompanied with an exothermic peak. The most probable associated chemical reaction is shown below in eqn (4.1):

$$NH_4ClO_4 \rightarrow NH_4^+ (s) + ClO_4^- (s) \leftrightarrow NH_3 (g) + HClO_4 (g) \qquad 4.1$$

Third and final decomposition of AP occurs at the temperature 380°C and is described as high temperature decomposition (HTD) and the peak is again exothermic in nature. This decomposition is caused by the oxidation of $NH_3$ by $ClO_4^-$ in gaseous phase and decomposition of AP on the solid surface of the catalyst. At the HTD, $HClO_4$ is converted into small molecules like NO, $O_2$, $Cl_2$, and $H_2O$ as shown below in eqn (4.2) and (4.3):

$$NH_4ClO_4 \rightarrow H_2O + NO_x + Cl_2 + N_2 + HCl \qquad (4.2)$$

$$HClO_4 \rightarrow H_2 + Cl_2 + O_2 + H_2O \qquad (4.3)$$

Thus, the AP showed the best decomposition behavior when modified with Cu-Cr-O.0.7$TiO_2$ calcined at 300°C. In general the modifier catalysts calcined at 300°C exhibited better effects on thermal decomposition of AP than the catalysts calcined at 1050°C. Crystallinity, surface properties, and specific surface area are the three key factors which determine the catalytic activity of the catalyst. In the present case, the most plausible reason behind the

superiority of the Cu-Cr-O samples calcined at 300°C over the similar samples calcined at 1050 °C may be as follows. During calcination at 300°C, only about 20 % of the precursor sample is decomposed as can be clearly seen in Fig. 4.1. Further decomposition of the remaining ~80% (above 300°C) alters the AP decomposition as shown in Fig. 4.16 as the crystallization temperature of Cu-Cr-O is 700°C. This is also reaffirmed by Fig. 4.4 and Fig.4.5 (FT-IR). The other factors behind this may be that at higher temperature (1050°C) the particles get diffused to each other and form comparatively larger particles of different surface morphology (see Fig. 4.6 and Fig.4.7) which results in the change in surface properties and a reduction in the specific surface area of the catalyst. Due to this reason, the Activity of the catalysts was found to be reduced ultimately at higher calcinations temperature. The catalyst samples prepared at 300°C has shown tremendously enhanced thermal decomposition of AP. Among them, the catalyst sample with 0.7 mol% $TiO_2$ (Cu-Cr-O.0.7$TiO_2$) exhibited unique decomposition (burn) rate of AP.

## 4.2 Effect of Reduced Graphene Oxide on the Catalytic Activity of Cu-Cr-O-$TiO_2$ to Enhanced the Thermal Decomposition Rate of Ammonium Perchlorate:

The effect of rGO on previously optimized Cu-Cr-O-$TiO_2$ system to enhance the burn rate of AP is very interesting idea. We have first optimized the concentration of $TiO_2$ in $CuO.CuCr_2O_4$ to get the best composite (Cu-Cr-O-0.7$TiO_2$) for improved thermal decomposition of AP and reported most recently [Kumar *et al.* 2017]. In the present investigations the effect of rGO into Cu-Cr-O-0.7$TiO_2$ system to enhance the thermal decomposition of AP as well as burn rate of SCP has been conducted. Aim of the present investigation is to achieve the highest burn rate of fuel at minimum possible temperature. In the present study, the rGO was synthesized and used for blending with ultrafine particles of $CuCr_2O_4$.0.7$TiO_2$ as synthesized by sol-gel method.

### 4.2.1 X-Ray Diffraction (XRD) Pattern of Synthesized Catalyst:

The crystalline phase and phase identification were carried out using XRD patterns of Cu-Cr-O-0.7$TiO_2$-rGO compositions as shown in Fig. 4.19. The characteristic diffraction peak for rGO with (002) as (hkl) values appears at the diffraction angle (2θ) of 26.1° matching with the JCPDS File No.03-0401 [Jeong *et al.* 2008 ;Yang *et al.* 2008]. The interlayer distance (d-spacing) between two layers is about 0.33 nm. The strongest diffraction peak appeared at 43.02° is due to copper chromite $CuCr_2O_4$ corresponding to the (400) plane (see the JCPDS File no. 26-0509). However, a weak peak appeared at 30.02° in the pattern is raised due to the (220) plane of the $CuCr_2O_4$ copper chromite.

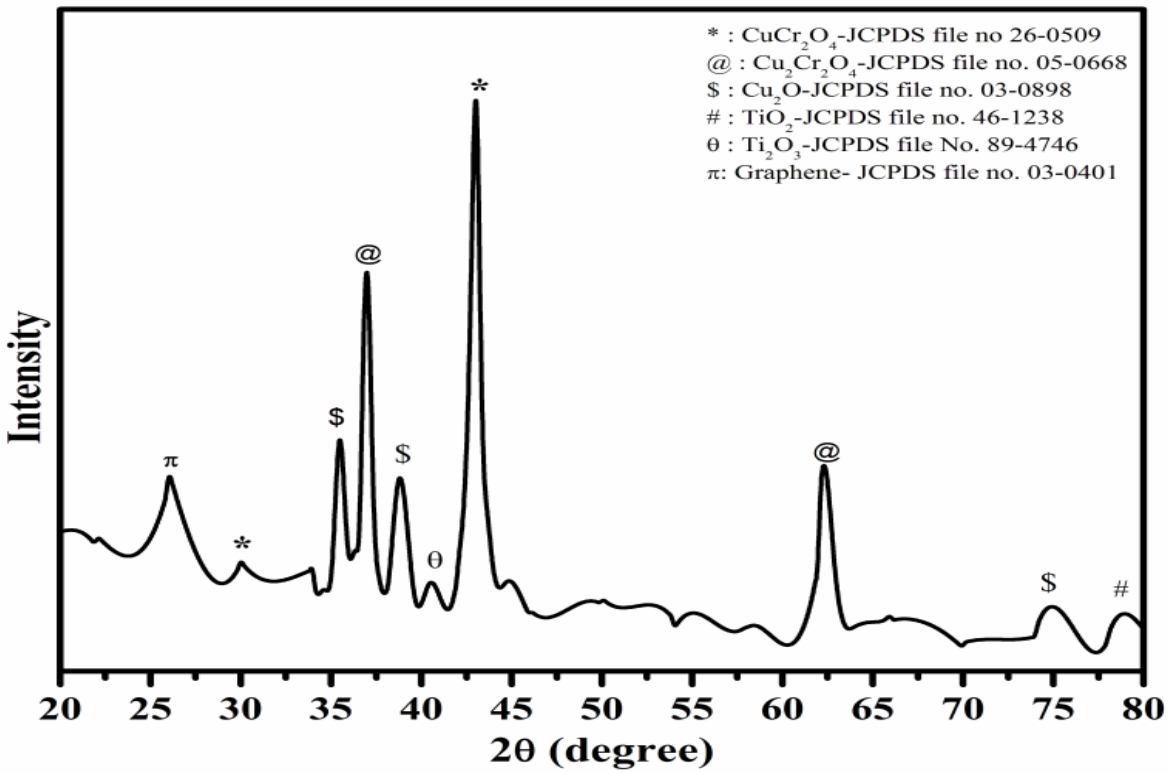


Fig. 4.19: XRD Pattern of Synthesized Catalyst

Secondary phase of copper chromite i.e. $Cu_2Cr_2O_4$ was also identified by the presence of the diffraction peaks at 36.98° and 62.30° with the corresponding planes (100) and (hkl), respectively as matched with JCPDS File no. 05-0668.

Diffraction peaks due to $Cu_2O$ have appeared at 35.48°, 38.82° and 75.23° with (111), (110) and (220) respectively as (hkl) values indexed with JCPDS File no. 80-4746. Titanium oxide was observed in two phase i.e. $Ti_2O_3$ (JCPDS File no. 89-4746) and $TiO_2$ (JCPDS File No. 89-4203) at the diffraction angles 40.54° and 78.94° with corresponding planes (113) and (117) respectively. The crystallite size of the synthesized catalyst were calculated by full width half maxima (FWHM) using the Scherrer formula as given below in equation (4.4).

$$d = \frac{0.9\lambda}{\beta \cos\theta} \qquad 4.4$$

d= crystallite size in nm, λ = wave length in nm, β is full width at half maxima and Θ is half of Bragg's angle. Crystallite size of the sample is observed to be 32 nm.

### 4.2.2 Infrared Spectroscopy of Synthesized Catalyst:

IR spectrum of Cu-Cr-O-0.7$TiO_2$-rGO catalyst sample is shown in Fig. 4.20 The strongest absorption envelope at 3430 $cm^{-1}$ is assigned to symmetric stretching mode of $OH^-$ [Mishra *et al.* 2016 ; Kaniyoor *et al.* 2014] Another strong shoulder observed at wavenumber 1641 $cm^{-1}$ appears due the C=C which is the characteristic shoulder of rGO. The position of this band may vary depending on the host molecule to which $H_2O$ is attached. The medium intensity bands recorded at 2926 and 2861 $cm^{-1}$ are attributed to the stretching vibrations of ν (C-H) of citric acid. The medium and sharp shoulder appearing at 1411 $cm^{-1}$ may be assigned to symmetric vibration of surface hydroxyl group. However, this band may also be attributed to $\nu_3$ carbonate ions ($CO_3^{2-}$). An un-indexed weak shoulder appearing at 1278 $cm^{-1}$ is attributed to the coupled bending and stretching vibrations of $COO^-$ of citric acid. Notably, citric acid has its melting point at 310 °C which is just above the 300 °C. That is why; citric acid is not destroyed at 300 °C [Kumar *et al.* 2017]. The shoulder at 1050 $cm^{-1}$ can be assigned to bending vibration of C-H of citric acid. The weak absorption bands observed at 892, 798 and 697 $cm^{-1}$ are attributed to the different vibrational modes of $TiO_2$ [Kumar *et al.* 2017]. $TiO_2$ exhibits strong absorption in the range 600-890 $cm^{-1}$ when treated with some other metal ions as in the present case. A broad absorption band centered at 538 $cm^{-1}$ is assigned to the characteristic vibrational band (asymmetric) of Cu-O in CuO as well as it also contains stretching bands of Cu-O-Cr [Kumar *et al.* 2017].

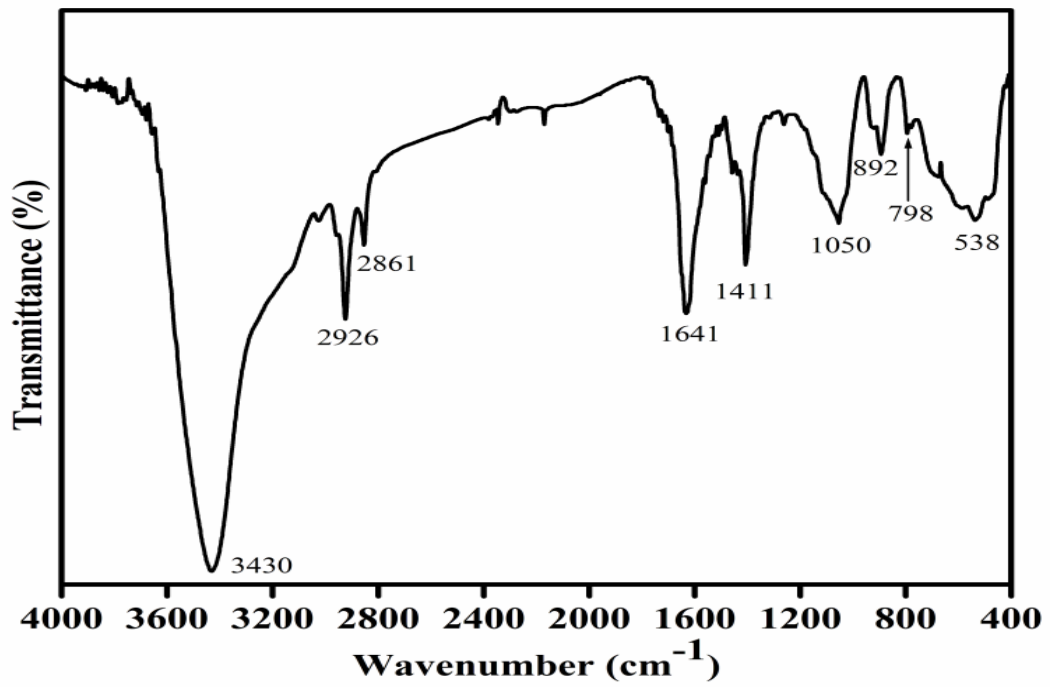


Fig. 4.20: FT-IR Pattern of Synthesized Catalyst

### 4.2.3 Raman Spectroscopy of Synthesized Catalyst:

Figure.4.21 shows the Raman spectrum of the synthesized composites of Cu-Cr-Ti-O-rGO recorded at room temperature. To avoid the decomposition of the sample, a laser of low power (5mW) was employed for recording the Raman spectrum. The spectrum is recorded between the wavenumber range 3000-300 $cm^{-1}$. The two most intense feature of Raman spectrum of rGO are the presence of a G band D bands and which are found to be present in this Raman spectrum. The G band is observed at ~ 1580 $cm^{-1}$ and this band always appears as the strongest band in the Raman spectrum as clearly shown in the Fig.4.21 [Kaniyoor *et al.* 2012 ; Kudin *et al.* 2008] Another significant mark of the Raman profile of rGO is the 2D band appearing at ~ 2700 $cm^{-1}$ as usually observed in graphitic structures. The zone-boundary phonons violate the Raman fundamental selection rule and consequently they give rise a peak at ~ 1352 $cm^{-1}$ in defected graphite as called D-band rather than the appearance of a Raman peak in the first order

Raman spectrum of defect-free graphite [Kaniyoor *et al.* 2012;Nemanich *et al.* 1979 ; Ferrari *et al.* 2006] .

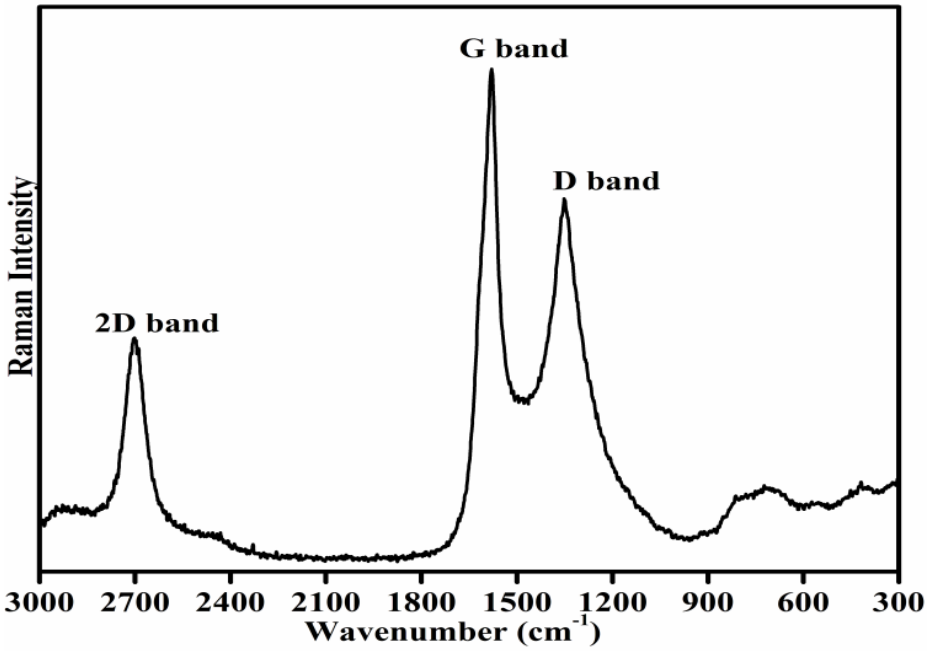


Fig.4.21: Raman spectrum of Synthesized Catalyst

The Raman spectrum of the graphene has a single sharp 2D peak. The number of layers in graphene is estimated based on the intensity of the 2D peak. Literature shows that as the increasing number of layers of graphene sheets, increases the intensity of the G band significantly, whereas it decreases the intensity of 2D band [Kaniyoor *et al.* 2012 ; Ferrari *et al.* 2006 ; Das *et al.* 2008 ; Cancado *et al.* 2008]. The position of D band in the present spectrum is noticed exactly at 1352 $cm^{-1}$. The G and D bands appear due to the doubly degenerate zone centre $E_{2g}$ mode at ~ 1580 $cm^{-1}$ and the breathing modes of six atom rings at 1352 $cm^{-1}$ because of the defects in the graphite. The recorded Raman profile containing the conventional and characteristics G, D and 2D bands at their defined positions with defined intensity convince the presence of graphene oxide in the prepared catalyst composite.

### 4.2.4 Scanning Electron Microscopy and Associated Energy Dispersive X-ray Analysis:

The surface morphology of the synthesized catalyst sample is shown in Fig. 4.22 (a-b). The microstructures of the sample at different magnifications (a) 2μm and (b) 1μm were carried out using the scanning electron microscopy technique operated at 10kV. The particles are formed to be spherical in shape and the particle size is in the range of 200-300 nm.

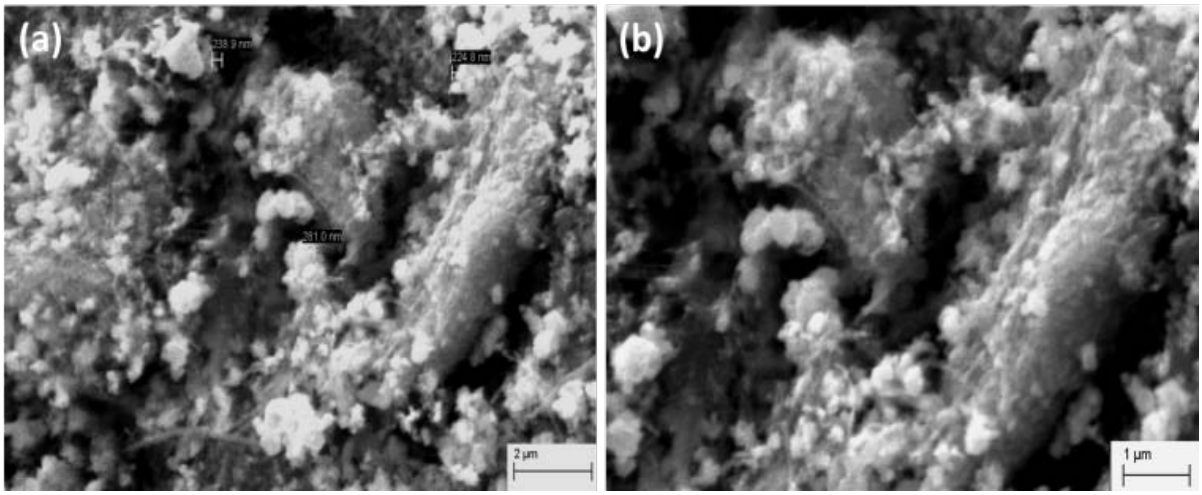


Fig. 4.22: SEM images of Synthesized Catalyst at (a) 1 μm and (b) 2 μm Magnifications

Elemental compositions of rGO added Cu-Cr-O-$TiO_2$ catalyst sample was carried out using EDX and observed atomic wt% of the constituent elements are shown in Table 4.4 This analysis confirmed the presence of carbon, copper, chromium, titanium and oxygen. The increasing weight % of oxygen with increase in the temperature may occur due to the transformation of intermediate compounds of Cu-Cr-O-Citric acid into metal oxides. Interestingly, CuO has already shown its presence in XRD patterns of the samples calcined at 1050°C not in the samples calcined at 300°C.

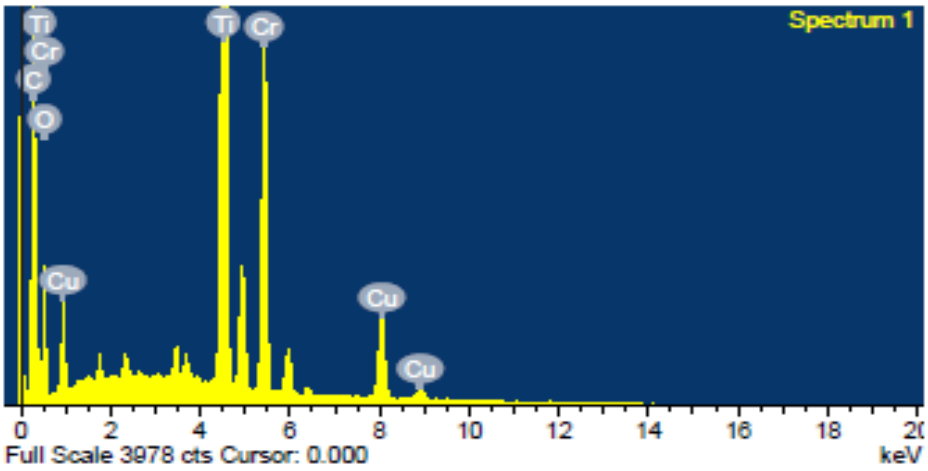


Fig.4.23: EDAX Spectrum of the Catalyst

**Table 4.4:** Elemental Composition of Synthesized Catalyst

| Elements | wt% |
|---|---|
| **C** | 38.33 |
| **O** | 13.21 |
| **Ti** | 26.13 |
| **Cr** | 13.89 |
| **Cu** | 8.44 |

### 4.2.5 Transmission Electron Microscopy (TEM) of Synthesized Catalyst:

Figure.4.24 shows the transmission electron microscopic images of Cu-Cr-O.0.7$TiO_2$-rGO composite sample calcined at 300 °C. Figure shows two images at two different magnification (a) 200 nm and (b) 20 nm, respectively with the selected area diffraction pattern (SAED) pattern shown as the inset image. At first glance on the images (a), the Cu-Cr-O-0.7$TiO_2$ particles of size around 100 nm can be seen easily in the yellow dotted yellow rings as shown by yellow arrows and rest of thing is the rGO as shown by bright brown arrows.

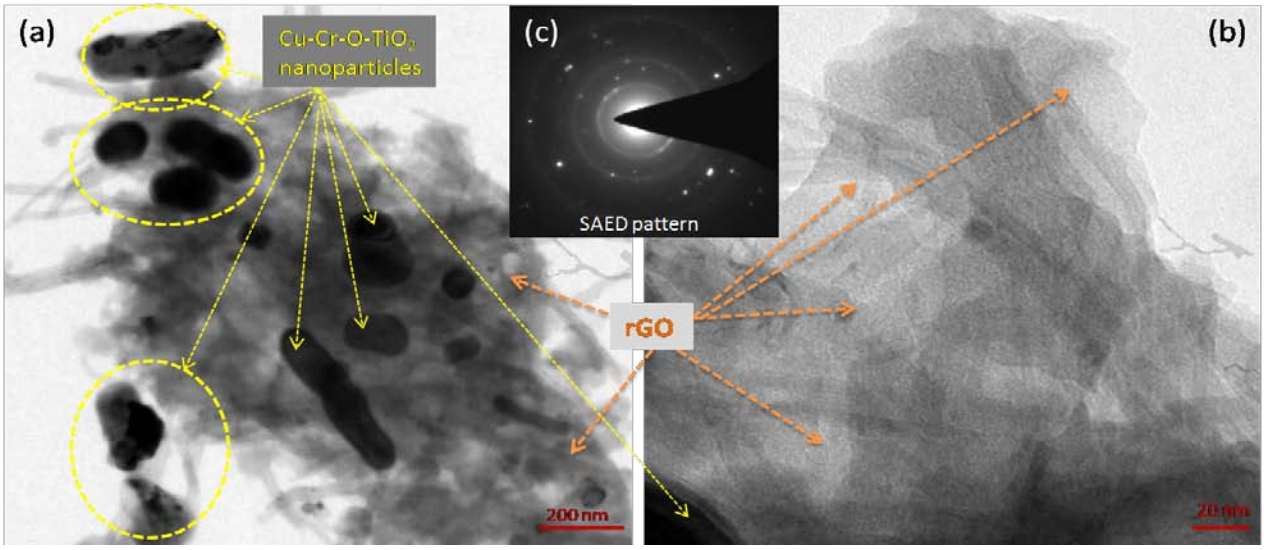


Fig. 4.24: TEM Images of Synthesized Catalyst at Two Different Magnifications (a) 200 nm and (b) 20 nm and (c) SAED Pattern as Inset Image.

A more clear view of rGO sheets is captured at higher magnification as shown in image (b). The Cu-Cr-O-0.7$TiO_2$ particles are scattered on the rGO sheets to form an organic-inorganic blend.

### 4.2.6 X-ray Photoelectron Spectroscopy (XPS):

The surface composition and oxidation states of the constituent elements of synthesized catalyst are represented by the characteristic core level spectra of Cu, Cr, Ti, O and C. XPS pattern of Cu as shown in Fig. 4.25. It is observed in two oxidation states namely $Cu^{+}$ and $Cu^{2+}$ in 72.24% and 27.76% respectively. The XPS spectrum of $Cu^{2+}$ as characterized by two spin orbit doublets with strong satellite peaks. The binding energies for Cu2p3/2 and Cu2p1/2 are 933.5 eV and 953.5 eV, respectively. Three satellite peaks with binding energies 941.5 eV, 944.03 eV and 962 eV are supporting the presence of CuO or mixed oxides CuO and $Cu_2O$.

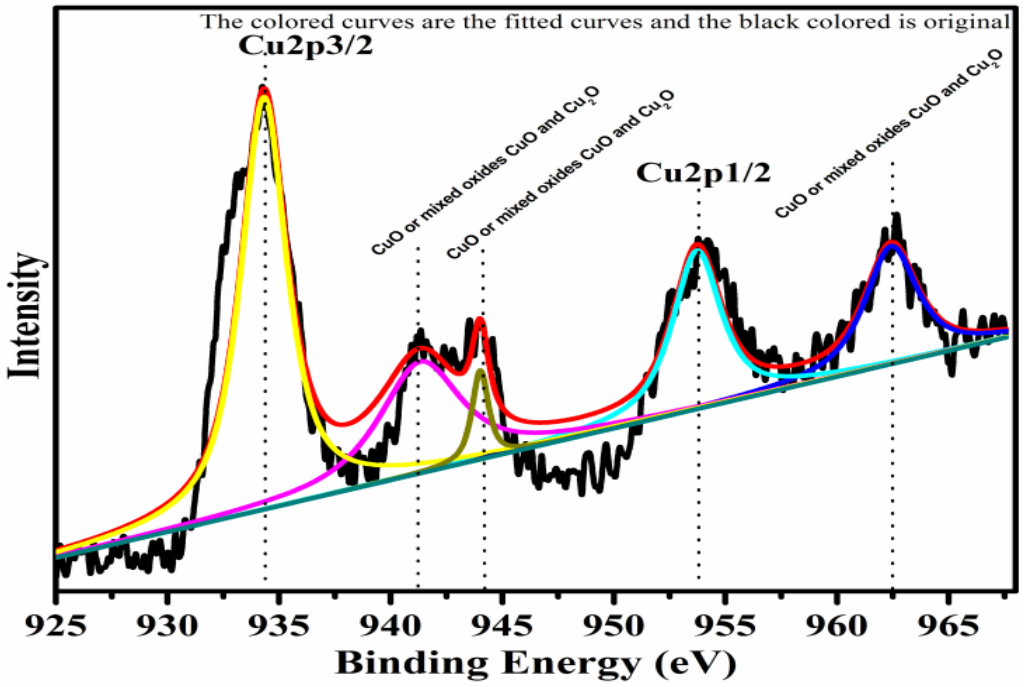


Fig. 4.25: XPS Pattern of Copper with Fitted Curves

The low energy component with $Cu2p_{3/2}$at 933.8 eV is associated with $Cu^{2+}$ in octahedron sites, where as high energy component at 935.3 eV is assigned to $Cu^{2+}$ in tetrahedral sites. XPS profile of Cr is shown in Fig 4.26. The XPS profile shows three peaks in which two appear with binding energies 586.4 eV corresponding to Cr2p1/2 and 576.07 eV corresponding to Cr2p3/2 [Aronniemi *et al.* 2005]. Third peak with binding energy 568.98 eV could not be assigned. The XPS profile of $TiO_2$ is represented in Fig 4.27. Titanium is observed in two different oxidation states i.e. $Ti^{2+}$ and $Ti^{4+}$ as 1.68% and 77.7% respectively. $TiO_2$ exhibits two peaks having binding energies 458.5 eV and 464.05 eV with their attribution to the $TiO_2$ 2p3/2 and $TiO_2$ 2p1/2. Figure 4.2.10 exhibits the XPS pattern of oxygen (O). Oxygen shows a peak with binding energy, 530.16 eV which is assigned to O1s. This peak is the main peak of oxygen which could be ascribed to the lattice oxygen in $TiO_2$.

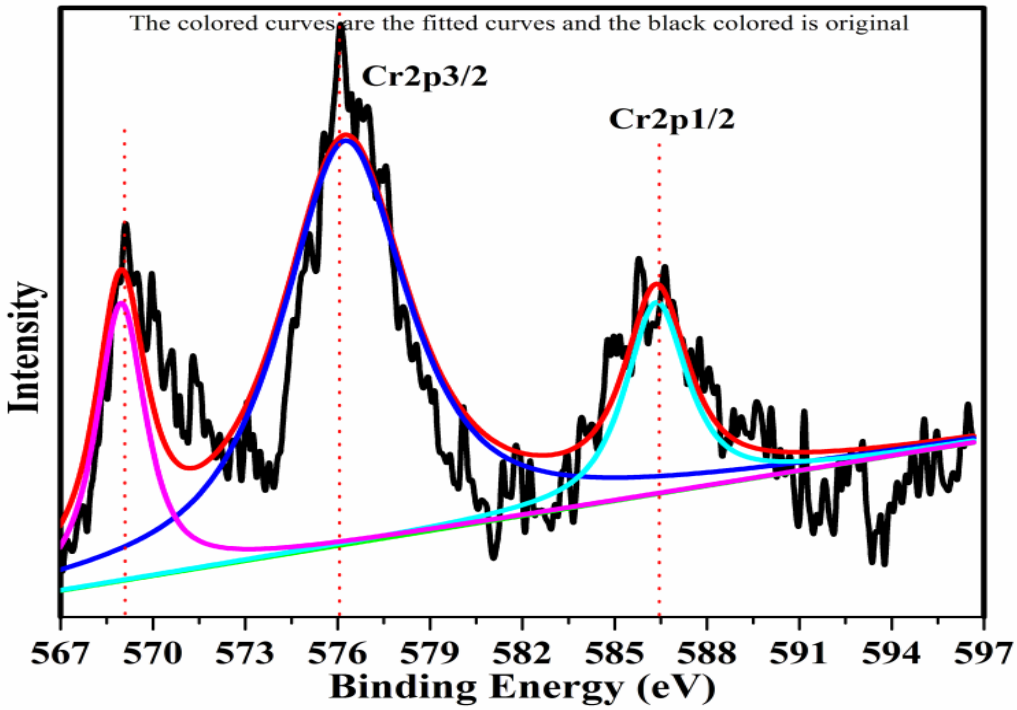


Fig. 4.26: XPS Pattern of Chromium with Fitted Curves

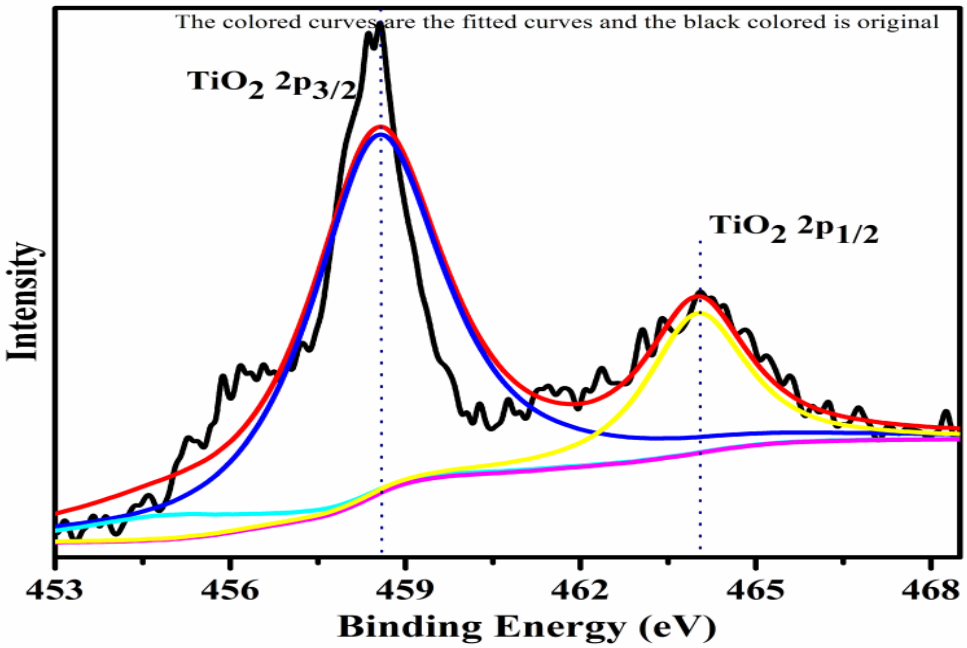


Fig. 4.27: XPS Pattern of Titanium Dioxide with Fitted Curves

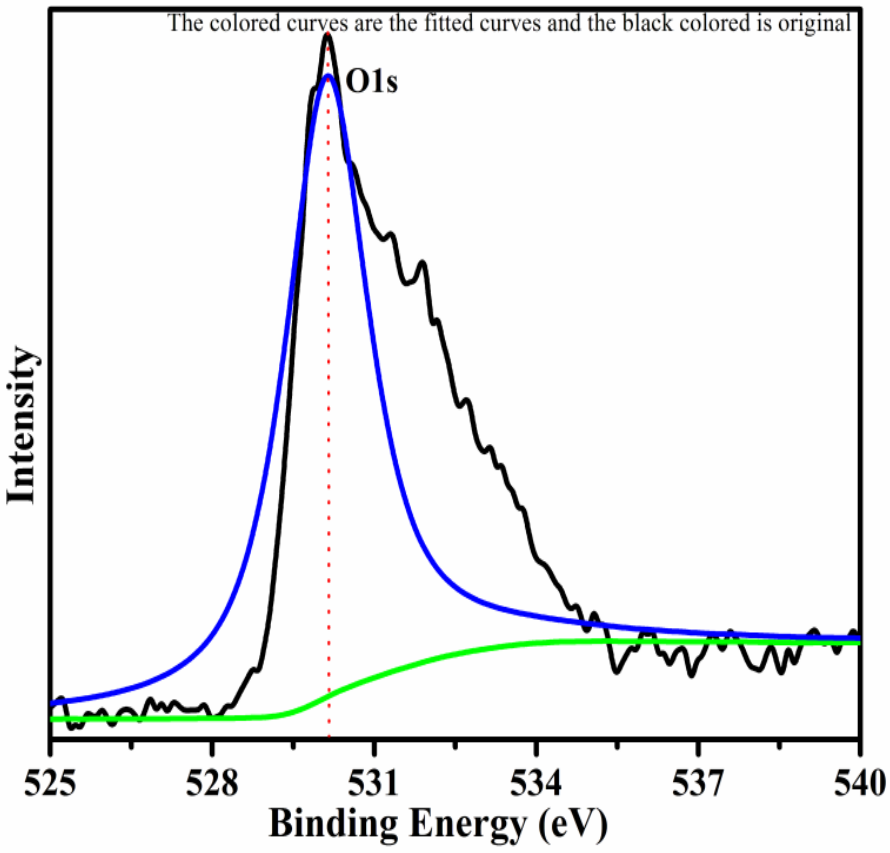


Fig. 4.28: XPS Pattern of Oxygen with Fitted Curves

XPS spectrum of carbon is shown in Fig 4.29. The C1s peak with binding energy 284.4 eV can be clearly seen in the pattern. This is the carbon of rGO used as additive in the catalyst. This C1s spectrum is taken as reference standard for peak shift correction of other elements by taking 284.eV as reference for C-C bond. The carbon is observed as asymmetric single bonded carbon (C-C) as $sp^2$ hybridization, the characteristic state of graphene. The XPS study also confirmed the presence of rGO due to maximum intensity peak at 284.4 eV (Fig. 4.29) which is associated to the asymmetric, single bond at sp2 hybridization of carbon [Neto *et al.* 2009].

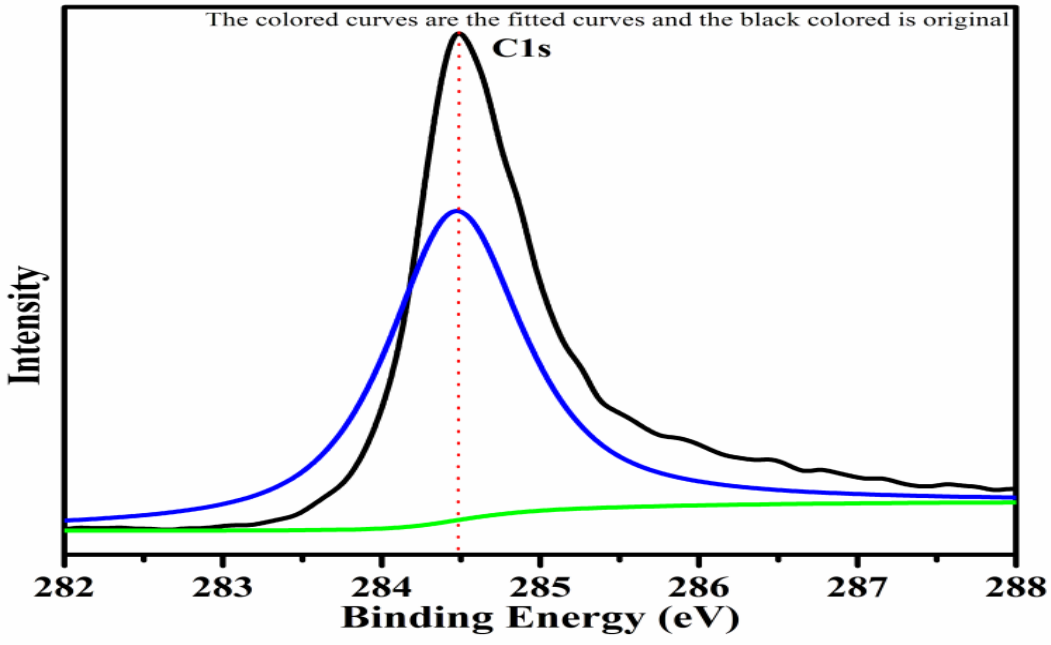


**Fig.4.29:** XPS Pattern of Carbon with Fitted Curves

### 4.2.7 Catalytic Activity:

#### 4.2.7.1 Effect of Synthesized Catalyst on Thermal Decomposition of AP:

The catalytic activity of as synthesized catalyst was carried out by thermogravimmetric and differential thermal analysis (TG-DTA) technique. DTA curve of pure AP is shown in Fig. 4.30 [Zhan *et al.* 2011]. According to curve, pure AP exhibits the first endothermic peak at the temperature 253°C associated with the crystallographic change of AP from orthorhombic to cubic. This is the characteristic crystallographic conversion of the AP [Zhan *et al.* (2011)]. Ammonium perchlorate exists in orthorhombic structure up to 230°C beyond which it gets transformed into cubic structure. The cubical structure of AP provides the comparatively dense packing and crystal defects resulting in faster rate of thermal decomposition and in turns, releases high energy during decomposition process [Shutton *et al.* 2000 ; Wang *et al.* 2011 ; Ping *et al.* 2006 ; Zhang *et al.* 2014]

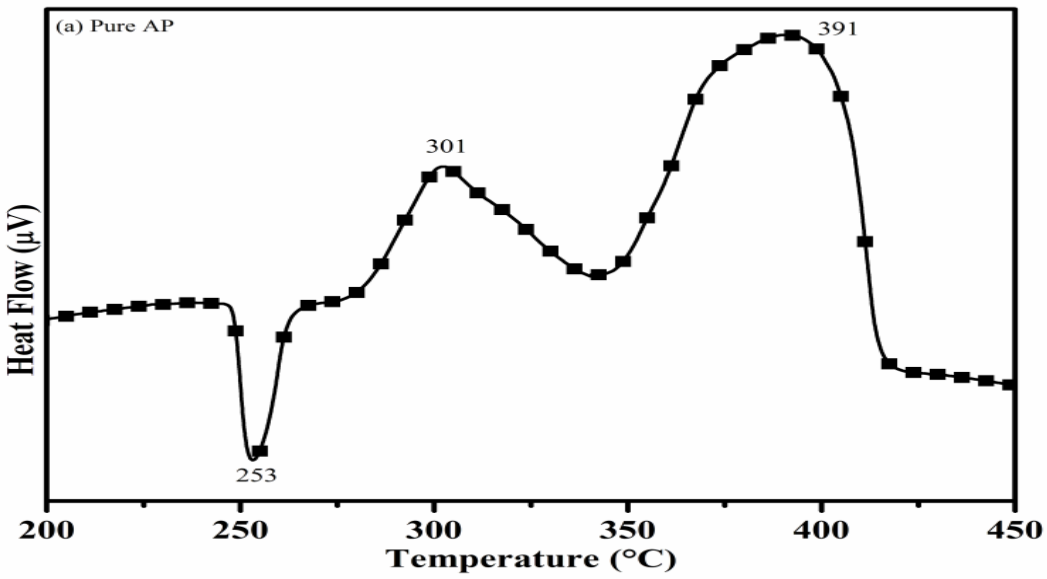


Fig.4.30: DTA Curve of Pure Ammonium Perchlorate (AP)

First exothermic peak or low temperature decomposition (LTD) is observed at 301°C. LTD is assigned to formation of intermediates i.e. decomposition AP into $NH^{4+}$ and $ClO^{4-}$ which consequently form ammonia ($NH_3$) and perchloric acid ($HClO_4$), respectively. The low temperature decomposition is governed by the electron transfer process. This decomposition is due to dissociation and sublimation and may be expressed through the following reaction equation (4.5)

$$NH_4ClO_4 \rightarrow NH_4^+(s) + ClO_4^-(s) \leftrightarrow NH_3(g) + HClO_4(g) \quad 4.5$$

The critical and most important factor governing the decomposition of ($NH_4ClO_4$) is above mentioned electron transfer process [Yan *et al*. 2009]. The systematic scheme is as follows.

$$NH_4ClO_4 \rightarrow NH_4^+ + ClO_4^- \quad 4.6$$

$$ClO_4^- \rightarrow ClO_4^0 + e^- \quad 4.7$$

$$NH_4^+ + e^- \rightarrow NH_3 + H(\text{atomic hydrogen}) \quad 4.8$$

$$H + ClO_4^0 \rightarrow HClO_4 \quad 4.9$$

$$HClO_4 + H \rightarrow H_2O + ClO_3^0 \quad 4.10$$

$$ClO_3^0 + e^- \rightarrow ClO_3^- \quad 4.11$$

$ClO_3^o$ acts as electron scavenger and converted into $ClO_3^-$.

The tri-metal composite of Cu-Cr-Ti-O (i.e. Cu-Cr-O-0.7$TiO_2$) with exhibits excellent property due the following proposed mechanism. Cu-Cr-O forms heterogeneous coupling with $TiO_2$ due to the suitable energy band gap. Cu-Cr-O is having 3d orbital structure and can simultaneously participate in the process of electron transfer. Cu-Cr-O releases the electron under stimulated condition and it induced the conduction band of $TiO_2$ resulting the actively participation of both Cu-Cr-O and $TiO_2$. The mechanism of electron release is as follows.

$$Cr^{3+} + ClO_4^- \rightarrow Cr^{2+} + ClO_4^0 \quad 4.12$$

$$Cr^{3+} + Cu^{2+}(3d^9) \rightarrow Cr^{3+} + Cu^{+}(3d^{10}) \quad 4.13$$

$$Cr^{3+} + Cu^{2+} \rightarrow Cr^{4+} + Cu^{+} \quad 4.14$$

$$Cr^{4+} + ClO_4^- \rightarrow Cr^{3+} + ClO_4^0 \quad 4.15$$

However, in case of Cu-Cr-O-$TiO_2$-rGOcomposite, rGO exhibits the excellent electrical and optoelectrical properties with n-type semiconducting nature [Giovannetti *et al.* 2008]. Due to its n-type semiconducting nature, it accepts the electrons released from $ClO_4^-$ and intermediates formed during the decomposition of ammonium perchlorate ($NH_4ClO_4$). A continuous electron transfer process from metal oxides and $ClO_4^-$ takes place. In Cu-Cr-O-$TiO_2$-rGO system, the Cu-Cr-O-$TiO_2$ being the p-type semiconductor releases the electron and rGO being the n-type semiconducting material accepts and facilitates the motion of those electrons released from Cu-Cr-O-$TiO_2$ more smoothly. Consequently, the electron transfer processes gets enhanced tremendously due to manifold high of electron mobility as compared to Cu-Cr-O-$TiO_2$ system and resulting in higher burn rate.

Second exothermic peak (or third i.e. final decomposition) of AP occurred at the comparatively higher temperature of 391°C. This one is known as high the temperature decomposition (HTD) peak. The HTD behavior is also exothermic in nature like LTD. HTD peak at 391°C is associated with the further decomposition of $H_2O$, HCl, $N_2$, $H_2$ and $O_2$. At high temperature decomposition, $HClO_4$ gets converted into small molecules and reaction is governed by the photon transfer process. The probable reactions are shown below in equation (4.16) and (4.17).

$$NH_4ClO_4 \rightarrow H_2O + NO_x + Cl_2 + N_2 + HCl \quad 4.16$$

$$NH_4ClO_4 \rightarrow H_2 + Cl_2 + O_2 + H_2O \quad 4.17$$

The particles of $CuCr_2O_4.0.7TiO_2$ have reduced the peak temperature of high decomposition with the merge of low temperature decomposition peak at faster rate. $CuCr_2O_4.0.7TiO_2$ has initiated the decomposition process by electron transfer followed by deprotonization of $HClO_4$ on solid surface in gaseous phase. During the decomposition, rGO has played vital role to accelerate the electron transfer.

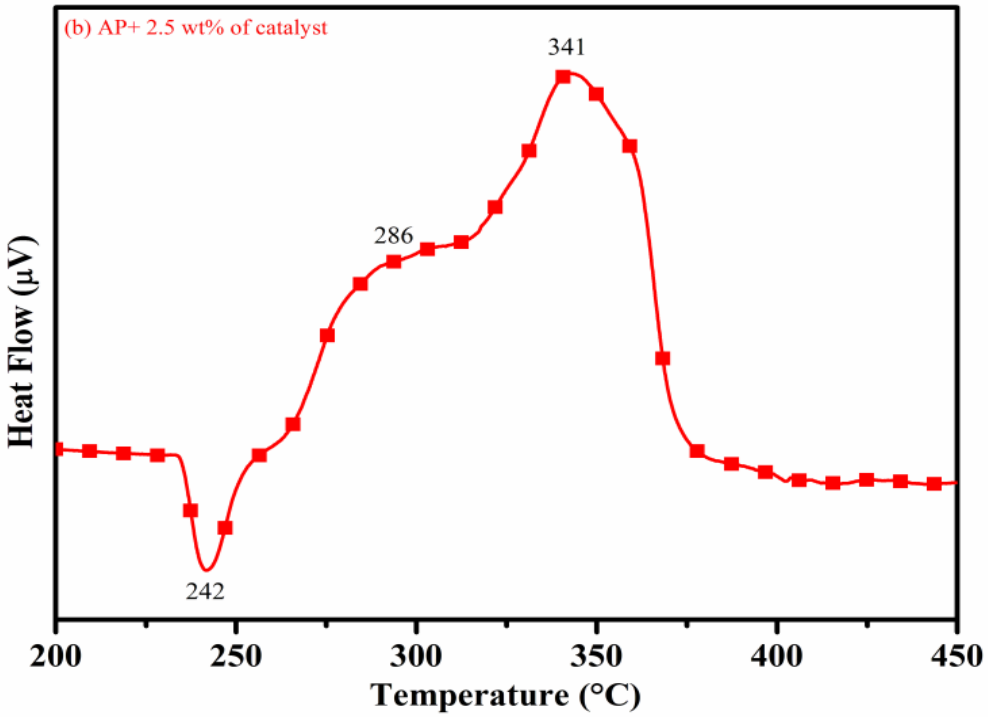


Fig.4.31: DTA Curve of AP Modified with 2.5 Wt % of Catalyst

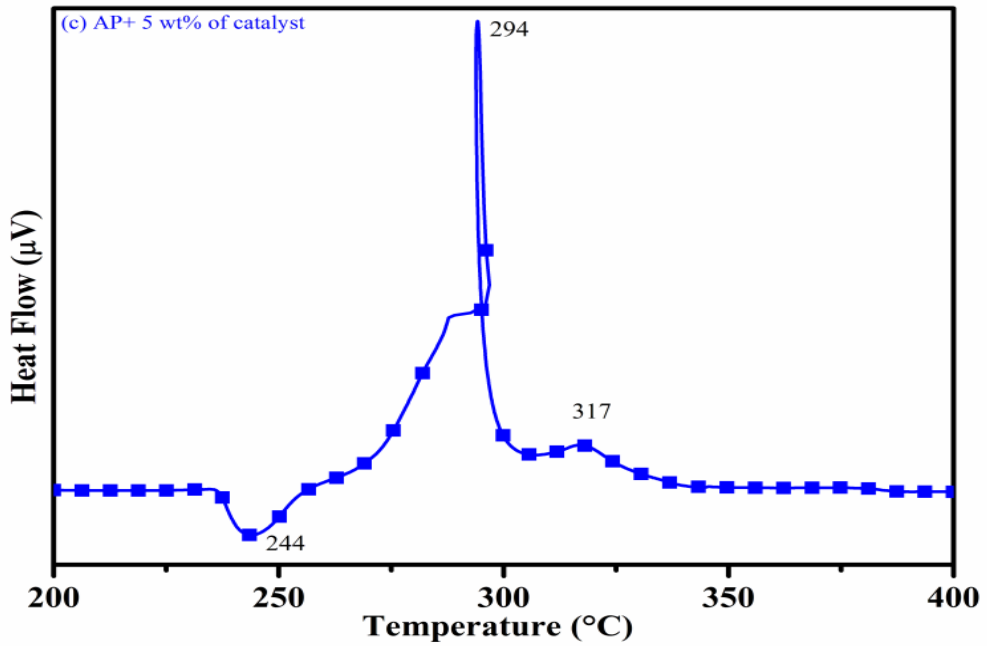


Fig. 4.32: DTA Curve of AP Modified with 5.0 Wt% of Catalyst

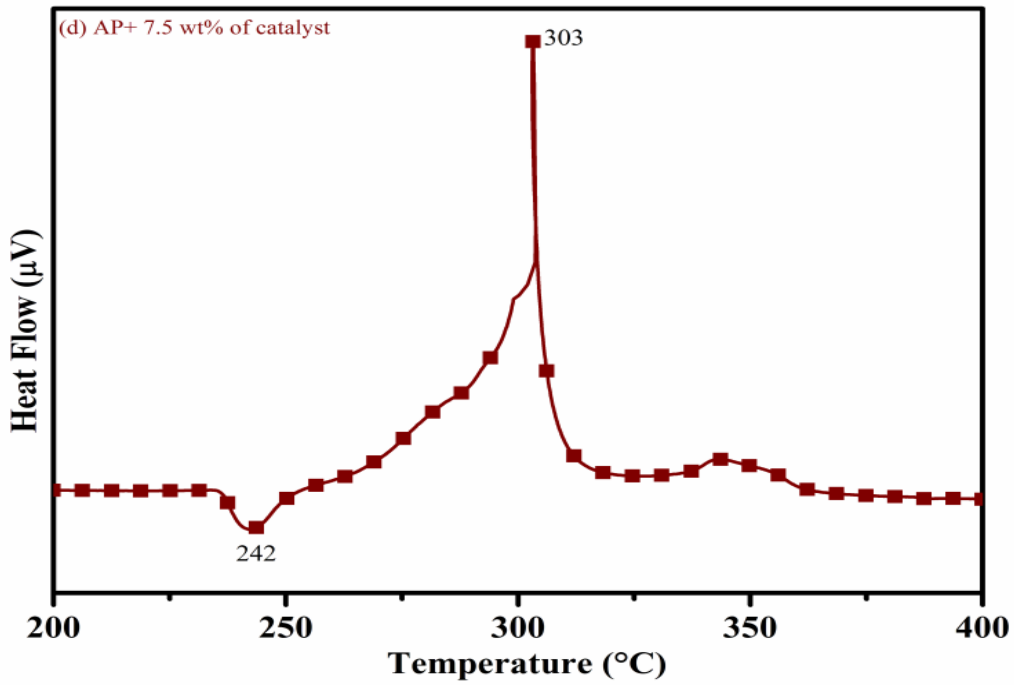


Fig. 4.33: DTA Curve of AP Modified with 7.5 Wt % of Catalyst

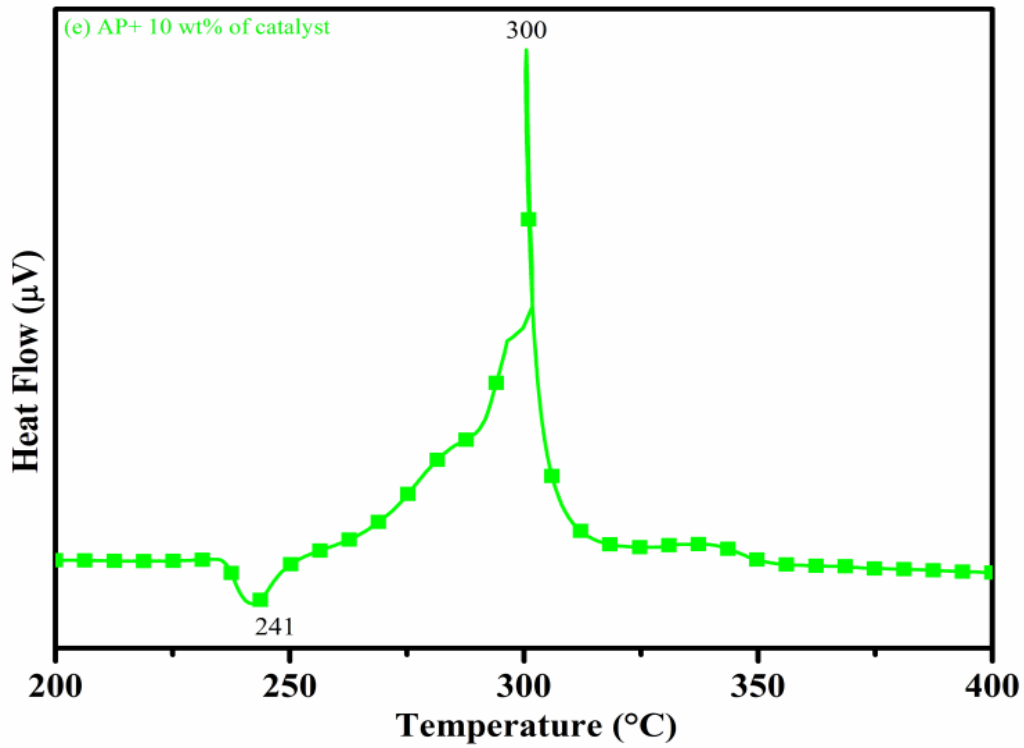


Fig. 4.34: DTA Curve of AP Modified with 10 Wt % of Catalyst

The DTA curves of AP modified with different (2.5, 5.0, 7.5 and 10) wt% of synthesized catalyst (Cu-Cr-O-$TiO_2$-GO) are shown in Fig. 4.31, Fig. 4.32, Fig. 4.33 and Fig. 4.34 respectively. A careful examination of first endothermic peaks in DTA curves of all the samples i.e. pure as well as modified AP permit to conclude that incorporation of catalyst additive in to pure AP significantly reduces the crystallographic transition temperature from 253°C to 242°C. The AP sample modified with least amount (2.5 wt%) of catalyst (Fig.4.31), the partial decomposition occurred at temperature of 286°C rather than 301°C with complete decomposition at 341°C rather than 391 °C as for pure AP.

Peak positions of LTD and HTD are reduced significantly by 15°C and 50°C respectively as compared to the pure AP. On the other hand, the separation between LTD and HTD is also reduced. More interesting results are observed when amount of catalyst is increased. As the 5 wt% of the synthesized catalyst is added into pure AP, both the LTD and HTD have been merged interestingly followed by single peak decomposition at 294°C as shown in Fig. 4.31. A tremendous lower shift of 97 °C of HTD and 7°C lower shift of LTD are noticed. The single stage decomposition of AP assisted with catalyst shows the spontaneous process of decomposition occurring within exceptionally less time interval. This graph contains a very small hump at 317°C which may be appearing due to infinitesimally small amount of $NH_4ClO_4$ or $HClO_4$ left in the sample. Amount of catalyst when further increased up to 7.5 wt% and 10 wt% into AP, the recorded thermal decomposition profiles of AP show single decomposition peaks at 303°C (Fig.4.33) and 300°C (Fig.4.34), respectively. Single stage peak decomposition positions for higher concentration of catalyst are shifted towards comparatively higher temperatures.

The addition of higher amount 7.5 wt% and 10 wt% of catalyst does not have a significant impact on thermal decomposition of AP as compared to 5 wt% amount of catalyst into AP. However, these samples (7.5 and 10 wt% of catalyst into AP) have much better than the industrial catalyst (ACR) as well as the previously reported catalysts [Kumar *et al.* (2017)].

Thus, excellent single stage decomposition of AP has been achieved at minimum temperature (294°C) with maximum decomposition rate (burn rate) in the presence of 5.0 wt% of synthesized catalyst material into AP.

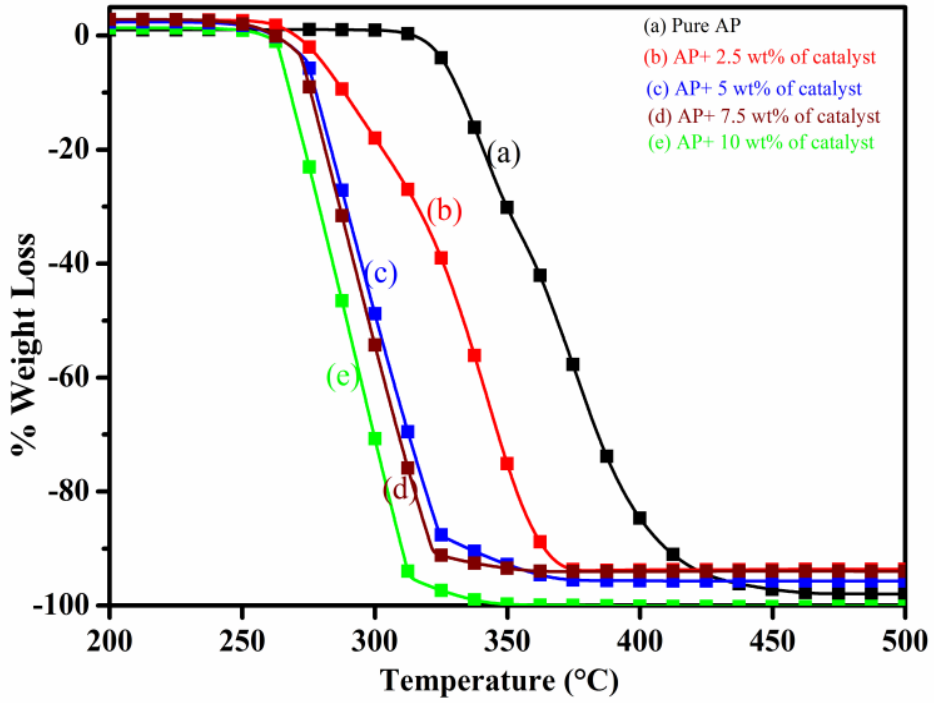


Fig. 4.35 (a-e): TGA Curves of the (a) Pure AP and AP with (b) 2.5, (c) 5, (d) 7 and (e) 10 wt% of Catalyst

Figure 4.35 (a-e) represents the TGA curves of the (a) pure AP and AP with (b) 2.5, (c) 5, (d) 7 and (e) 10 wt% of synthesized catalyst (Cu-Cr-O-$TiO_2$-rGO) recorded in the temperature range of 200-500°C. TGA curves of all the samples are in line with the corresponding DTA curve.

TGA curve shows the change in % weight loss of the sample in the temperature range of 260 to 380°C. Beyond 380°C, TGA curve becomes straight which clearly explains the completion of thermal decomposition of ammonium perchlorate.

### 4.2.8 Effect of Synthesized Catalyst (Modified AP) on Burn Rate of Solid Composite Propellant (SCP):

The combustion activity of the SCP is the function of the stoichiometry of the propellant ingredients. Since, major ingredient (68 wt %) of SCP is AP so, thermal decomposition AP is the major factor to decide the combustion activity of SCP. Furthermore, the thermal decomposition of AP is strongly depends on the presence of catalyst as well as on particle size and shape of AP. A change in thermal decomposition of AP will ultimately affect the burn rate of SCP. Better the thermal decomposition of AP, higher the burn rate of SCP. In the present study, the thermal decomposition of AP has been found to get enhanced remarkably by using the different concentrations of synthesized catalyst mixed thoroughly into AP. The activities of synthesized and commercial (ACR) catalysts are determined in terms of the burn rate of SCP. Higher the burn rate at low temperature with the lower exponent on the pressure is the desired requirement. The governing burn rate equation, $r = a\,p^n$, discussed earlier (cf. Section 1.9 , Eq.1.18 ) has been used for calculating the burn rate. The burn rate of the SCP is evaluated at the combustion pressure of 33 bar using acoustic measurement method through strand burner as shown below in Fig. 4.36 (a).

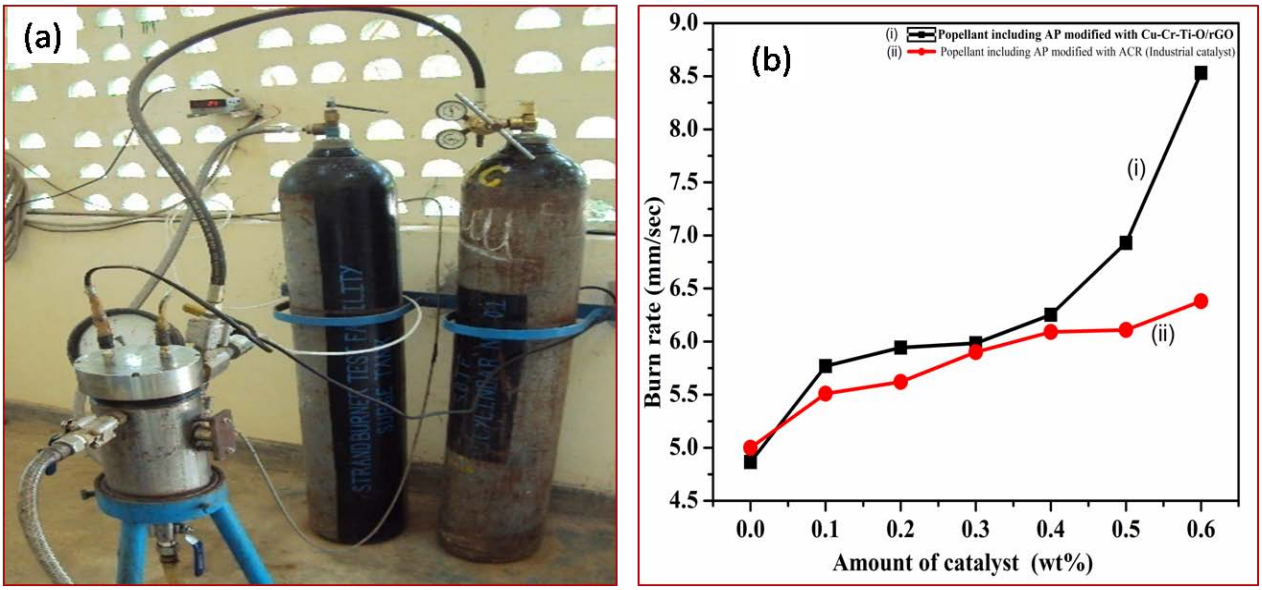


Fig. 4.36: (a) Images of Strand burner (b) Burn rate of (i) SCP having AP modified with synthesized catalyst and (ii) SCP having AP Modified with Industrial Catalyst

The burn rate curves of SCP having AP modified with synthesized catalyst and AP modified with industrial catalyst are shown in Fig. 4.36 (b). The excellent catalytic effect is observed in presence of 5 wt % of $CuCr_2O_4.0.7TiO_2$-rGO catalyst in AP. A tremendous increase (175.31 %) in burn rate of SCP is observed at 0.6 wt % of synthesized catalyst (8.531 mm/sec) in AP as compared to pure AP (4.866 mm/sec). The burn rate of SCP is noticed to be 133. 61% for AP modified with industrial catalyst ACR (6.385 mm/sec). The obtained faster rate decomposition of AP in single stage can be considered as the explosive reaction, which is supported by auto-ignition process.

## 1.3 Kinetic Study of Thermal Decomposition of Ammonium Perchlorate (AP):

Thermal decomposition of energetic materials like propellant and explosive is significantly important as the performance of propulsion system depends upon their decomposition behavior. Ammonium perchlorate, being one of the major stake holder (~70-75 wt.%) of solid composite propellant as well as known as monopropellant, became the crucial ingredient to be studied well in terms of the thermal stability. The thermal stability is an important parameter which determines the storage life, deterioration in the oxidative property and sensitivity against the impact or spark.

Basically AP based solid composite propellant is being used in the space vehicles, ballistic missiles and to some extant in the tactical missiles. The reason for the world wide use of ammonium perchlorate as an oxidizer is due to its high oxygen content, large specific volume of the product gases and extensive handling and storage experience [Jacob *et al.* 1969]. The kinetic study of thermal decomposition of ammonium perchlorate in presence of synthesized catalyst became significantly important as the rate of decomposition turns into spontaneous decomposition process and gets decomposed in a single stage at a much lower temperature (294°C) where as pure AP decomposes in two major temperature steps (LTD and HTD) at 301 and 391°C, respectively. The different methods which are employed for investigating the kinetic parameters are discussed here.

### 4.3.1 Kissinger Method:

The activation energy of thermal decomposition of ammonium perchlorate can be calculated by using the Kissinger equation (Kissinger, 1957). According to this equation $\mathbf{ln}\left(\frac{\boldsymbol{\beta}}{\mathbf{T_P}^{\mathbf{2}}}\right)$ is linearly related to the $1/T_p$ as given below:

$$\ln\left(\frac{\beta}{T_P{}^2}\right) = \ln\left(\frac{A.R}{E_a}\right) - \frac{E_a}{R.T_p} \qquad 4.19$$

where $T_p$ is the peak temperature (K), β is the heating rate ($K.min^{-1}$), $E_a$ is the apparent activation energy ($kJ.mol^{-1}$), R is the ideal gas constant and A is the pre-exponential factor. The above mentioned equation is valid with the reaction order of 1 (n=1). When the reaction order is not 1 then the following Kissinger equation is used to evaluate the activation energy of thermal decomposition.

$$\ln\left(\frac{\beta}{T_P{}^2}\right) = \ln\left(\frac{C_0^{n-1}.A.R}{E_a}\right) - \frac{E_a}{R}.\frac{1}{T_p} \qquad 4.20$$

for $n > 0$ and $n \neq 1$.

The graph between $\ln\left(\frac{\beta}{T_P{}^2}\right)$ and $1/T_p$ gives the straight line. The activation energy is calculated by using the slope of the straight line. When the activation energy is calculated by using either one of the equations depending upon the order of reaction, pre-exponential factor can be evaluated using the following the relation.

$$A = \left\{\beta E_a \exp\frac{E_a}{RT_p}\right\} \Big/ RT_p^2 \qquad 4.21$$

The rate constant of the reaction cab be calculated using the Arrhenius equation as given below.

$$K = A \exp\left(-\frac{E_a}{R.T_p}\right) \qquad 4.22$$

The enthalpy of activation can also be calculated once the activation energy is known by using relation:

$$\Delta H^{\neq} = E_a - RT_p \qquad 4.23$$

### 4.3.2 Ozawa – Flynn – Wall (OFW) Method:

Ozawa – Flynn – Wall method for evaluating the kinetic parameters of the reaction is a model free approach. This method is based on the basic kinetic equations and can be applied for any kind of material. This method is also known as the isoconversional method and allows model free approach for the estimation of activation energy [Ozawa – Flynn – Wall, 1965}. The following is the correlation used for estimation of activation energy:

$$\ln \beta = \ln\left(\frac{A.E_a}{Rg_{\propto}}\right) - 5.523 - 1.0518\left(\frac{E_a}{RT_p}\right) \qquad 4.24$$

The graph is plotted between $1/T_p$ and $\ln\beta$ at the different heating rates, gives a linear relationship for the specified conversion ($\alpha$). From the slope of the straight line activation energy is calculated.

The Kissinger (1957) and Ozawa-Flyn-Wall (1965) methods differ in the procedure used for solving temperature integral. Kissinger solved the temperature integral using the approximation given by

$$g(x) = \exp(-x)\,(1-2x^{-1})\,x^{-2}$$

where x is $E_a/RT$. Ozawa-Flyn-Wall on the other hand used Doyel's approximation [Doyle, 1961, 1962, 1965] given by

$$g(x) = \exp(-1.0518x - 5.550)$$

### 4.3.3 Kissinger-Akahira-Sunose Method:

This is the modified version of Kissinger method in which temperature of specific conversion is used in the equation instead of decomposition peak temperature ($T_p$). The correlation is as below.

$$\ln\left(\frac{\beta}{T_{\alpha}^2}\right) = \ln\left(\frac{A.R}{g(\propto)E_a}\right) - \frac{E_a}{RT_{\propto}} \qquad 4.25$$

### 4.3.4 Friedman Method:

Freidman proposed a method which became very much popular and is being widely used by the scientific and researchers community for the isoconversional kinetic analysis of different materials. This method also provides the model free approach and used to determine the number of activation energy for different degree of conversion [Freidman, 1964]. The correlation is given as below.

$$\ln\left(\beta\frac{d(\alpha)}{dT}\right) = \ln\left[Af(\alpha)\right] - \frac{E_a}{RT} \qquad 4.26$$

The differential method proposed by Friedmann and integration methods proposed by Kissinger and OFW are used to parameterize the thermal analysis kinetic data for non-isothermal conditions. The Friedmann method is numerically unstable and noise sensitive, especially when the reaction kinetics is parameterized by numerical differentiation of the experimental data. Kissinger and OFW methods are limited by the use of linear variation in temperature and positive heating rate. Thus these are not applicable for cooling, which is essential for the study of crystallization kinetics of melts [Sbirrazzuoli, 2007].

### 1.3.5 Kinetic Study:

In the present work the kinetic study was carried out using the differential thermo- gravimetric (DTA) analysis in the inert atmosphere. The modified Kissinger method was adopted for calculating the kinetic parameters i.e activation energy, reaction rate constant and pre-exponential factor. The DTA analysis of AP in presence of catalyst was carried out at different heating rates (i.e. 10, 20, 30 and 40°C/min.) in an inert atmosphere. The DTA curves at different heating rates exhibit the thermal decomposition behavior of ammonium perchlorate differently

indicated by the shift in decomposition peaks. The decomposition peak shifted towards the higher value at higher heating rate which may be because of the lesser residence heating time of the sample while increasing the heating rate. At a heating rate of 10°C/min, the peak appeared at 294°C where as peaks appeared at 304, 311 and 340°C corresponding to the heating rates of 20, 30 and 40°C/min, respectively. A logarithmic graph was plotted between $\ln\frac{\beta}{T_p^2}$ and $\frac{1}{T_p}$, where $T_p$ is the decomposition peak temperature (K). The linear relationship between $\ln\frac{\beta}{T_p^2}$ and $\frac{1}{T_p}$ was obtained. The slope of the curve represents the ratio $\frac{E_a}{R}$ and accordingly the activation energy ($E_a$) of thermal decomposition of ammonium perchlorate was calculated. Further equating the intercept of the graph with the Y axis to $\ln\left(\frac{A*R}{E_a}\right)$ provides the value of pre-exponential factor or frequency factor. After arriving at the value of activation energy and pre-exponential factor Arrhenius equation has been used to calculate the reaction rate constant. Jacob *et al.* (1969) ; Boldyrev, (2006) and Vyazovkin *et al.* (1999) investigated the kinetic parameter of thermal decomposition of ammonium perchlorate using the Kissinger method and observed the activation energy of low decomposition temperature of AP in the range of 80 to 115 KJ/mol where as activation energy of high temperature decomposition was in the range of 150 to 260 KJ/mol. Pesina *et al.* (2017) studied the thermal decomposition of ammonium perchlorate-aluminum propellants in presence of metallic zinc particles and concluded that the activation energy of pure AP decomposition is 91 and 229 kJ/mol for LTD and HTD, respectively where as in presence of 10wt% of Zn particle the activation energy came down to 56 KJ/mol for the exothermic peak.

Figure 4.37 show the DTA curves of thermal decomposition of ammonium perchlorate in presence of 5wt % of Cu-Cr-O-0.7$TiO_2$-rGO at the different heating rates of 10, 20, 30 and 40°C/min. The data for plotting the Kissinger graph is given in Table 4.5.

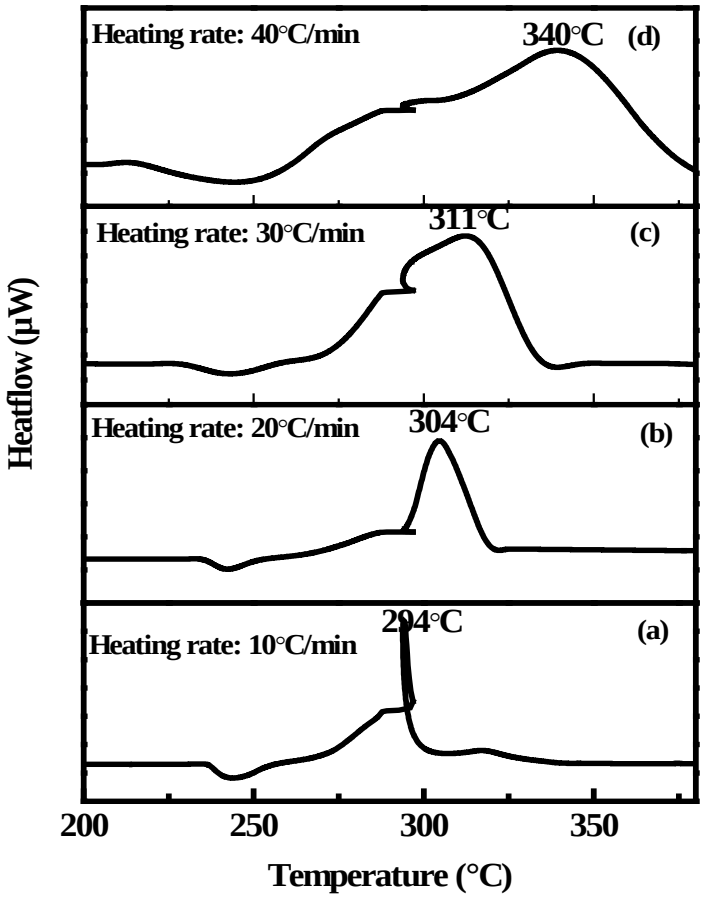


Fig.4.37: DTA Curves of AP with 5wt% of Catalyst (a) at a Heating Rate of 10°C/Min (b) Heating Rate of 20°C (c) Heating Rate of 30°C and (d) Heating Rate of 40°C

**Table 4.5:** Kinetic data of thermal decomposition of AP in presence of 5 wt% of synthesized catalyst

| **Heating Rate, (β, °K/min)** | **Peak temperature ($T_p$,°K)** | **1/ $T_p$** | **1/ $T_p^2$** | **β/ $T_p^2$** | **ln(β/ $T_p^2$)** |
|---|---|---|---|---|---|
| 10 | 567 | 0.00176 | $3.09 X10^{-6}$ | $3.09 X10^{-5}$ | -10.384 |
| 20 | 577 | 0.00173 | $2.99 X10^{-6}$ | $5.98 X10^{-5}$ | -9.7245 |
| 30 | 584 | 0.00171 | $2.92 X10^{-6}$ | $8.76 X10^{-5}$ | -9.3427 |
| 40 | 613 | 0.00163 | $2.66X10^{-6}$ | $1.64 X10^{-4}$ | -8.7156 |

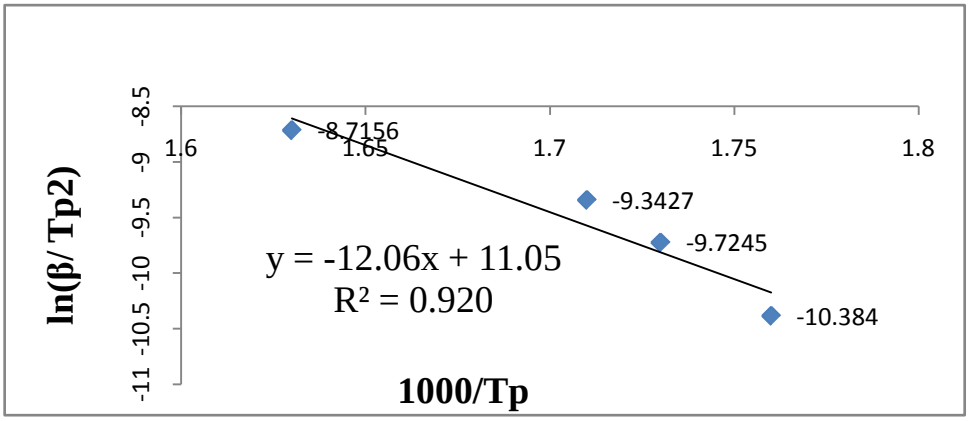


Fig. 4.38: Kissinger graph between $\frac{1000}{T_p}$ and $\ln\frac{\beta}{T_p^2}$

### 4.3.5 Calculation of Activation Energy of Thermal Decomposition of AP:

$$\frac{E_a}{R} = 12.06$$

$$E_a = 12.06 * R$$

$$E_a = 12.06 * 8.314 \ (JK^{-1}mol^{-1})$$

$$E_a = \ 100.266 \ (kJmol^{-1})$$

### 4.3.6 Calculation of Pre-Exponential Factor:

From the graph the intercept value is arrived and by using the following relation the pre-exponetial factor was calculated.

$$\ln\left(\frac{A * R}{E_a}\right) = 11.5$$

$$A * R = E_a * e^{11.5}$$

$$A * R = 98715.77 * 1000$$

$$A = 11873438.777$$

$$A = 1.18x10^{7}S^{-1}$$

### 4.3.7 Calculation of Reaction Rate Constant:

$$K = A \exp\left(-\frac{E_a}{R.T_p}\right)$$

$$K = 11873438.777\exp\left(-\frac{100.266 * 1000}{8.314 * 567}\right)$$

$$K = 11873438.777x5.7883711x10^{-10}$$

$$K = 0.006827S^{-1}$$

**Table 4.6:** Summery of kinetic parameters

| **Kinetic Paramters** | **Value** |
|---|---|
| Activation Energy ($E_a$) | 100.266 kJ $mol^{-1}$ |
| Pre-exponential factor (A) | 1.18 x $10^{7}$ ($s^{-1}$) |
| Reaction rate constant (k) | 0.006827 ($s^{-1}$) |

Table 4.6 summerizes the kinetic paramters of thermal decomposition of AP in presence of 5wt% of Cu-Cr-O-0.7$TiO_2$-rGO catalyst. The activation energy of the thermal decomposition of

AP obtained through this work is in well agrrement with the value reported by other coworkers as listed below in table 4.7.

**Table 4.7** the comparison of kinetic parameters for different compositions in presence of different catalyst as reported in available literature

| S.No. | Composition | ($E_a$), kJ/Mol | A ($min^{-1}$)/*lnA* | K ($s^{-1}$) | Reference |
|---|---|---|---|---|---|
| 1. | Pure AP | 324.24 | $4.31X\ 10^{27}$ | $5.61X10^{-4}$ | Patil, P. *et al.* (2008) |
| | AP+ 2% Commercial CuO | 274.24 | $2.79\ X\ 10^{20}$ | $6.81X\ 10^{-4}$ | |
| | AP+ 2% commercial $CuCr_2O_4$ | 238.3 | $1.01\ X\ 10^{17}$ | $5.48\ X\ 10^{-4}$ | |
| | AP+ 2% nano CuO | 120.13 | $2.84\ X\ 10^{9}$ | $5.99\ X\ 10^{-3}$ | |
| | AP+ 2% nano $CuCr_2O_4$ | 100.24 | $7.89\ X\ 10^{7}$ | $4.44\ X\ 10^{-3}$ | |
| 2. | AP+ Cu@h-BN | 197 | - | - | Huang, C. *et al.* (2015) |
| 3. | Pure AP | 100 (LTD)/177(HTD) | | | Chaturvedi, S. et.al., (2013) |
| | AP + Cu (90nm) | 93/155 | | | |
| | AP + Ni (50nm) | 111/167 | | | |
| | AP + Al (30nm) | 121/172 | | | |
| | AP + NiCu (45nm) | 106/154 | | | |
| 4. | Pure AP | 178.1 | $2.3\ X\ 10^{11}$ | 0.015 | Zhao, S. et. al., (2010) |
| | AP + 5% $CoFe_2O_4$ | 106.5 | $2.9\ X\ 10^{9}$ | 0.514 | |
| | Pure AP | 1540±13.9 | *26.8* | | Zhaou, Z. et. al., |
| | AP + $ZnCl_2$ ) (100:2) | 937± 22.4 | *18.4* | | |

| | | | | | |
|---|---|---|---|---|---|
| 5. | AP + $ZnCl_2$ ) (100:4) | 965±15 | *20* | | (2012) |
| | AP + $ZnCl_2$ ) (100:6) | 142±21.0 | *29.4* | | |
| 6. | Pure AP | 49.14 | *4.65* | | Singh, G. *et al.* (2009) |
| | AP + Cobalt Ferrites | 36.01 | *2.42* | | |
| | AP + Copper Ferrites | 41.29 | *3.32* | | |
| | AP + Nickel Ferrites | 43.28 | *3.64* | | |
| 7. | Pure AP | 124 | | | Fujimura, K. et. al., (2010) |
| | AP + $TiO_2$ (A) | 115 | | | |
| | AP + $TiO_2$ (B) | 123 | | | |
| | AP + $TiO_2$ (C) | 139 | | | |
| | AP + $TiO_2$ (D) | 133 | | | |
| | AP + $TiO_2$ (E) | 123 | | | |